Inclusion of Phase Information into the Image Source Method

Master thesis by
Eduardo Fonseca Montero

Section of Acoustics - Department of Electronic Systems
Aalborg University 2009

Department of Electronic Systems
Section of Acoustics
Fredriks Bajers Vej 7
http://es.aau.dk/sections/acoustics/

Title:

Inclusion of Phase Information into the Image Source Method

Theme:

Master thesis

Project period:

February 1st - June 3rd, 2009

Project group:

09gr1061

Participants:

Eduardo Fonseca Montero

Supervisor:

Daniela Toledo

Copies: 2

Number of pages:

-In main report: 79

-In appendix: 9

Enclosures: CD

Date of completion: June 3rd, 2009

Abstract:

In this project the conventional image source method is modified by including the phase information in order to allow for interference phenomena. This is performed by incorporating complex sound pressure propagation while keeping real reflection coefficients. This phase image source method is used to compute the simulated pressure impulse responses of a modelled room consisting of a quasi rectangular geometry with acoustically hard surfaces.
The performance of the implemented model is assessed in both time and frequency domains by comparing the simulation results with measurements carried out in the real room.
It is shown that the implemented model provides reasonably accurate predictions of the complex sound field in the considered scenario at the medium frequency range and for the early part of the impulse responses.

Preface

This Master thesis is written by project group 09gr1061 at the Section of Acoustics, Department of Electronic Systems at Aalborg University during the 4th semester of the Master programme in the period spanning from February 1st, 2009 to June 3rd, 2009. The project concerns the development and evaluation of a method for simulation of the sound field in rooms.

The report is aimed at people with knowledge equivalent to the teaching on a Master programme in acoustics. The project "Inclusion of Phase Information into the Image Source Method" has been proposed by the author in conjunction with the supervisor Daniela Toledo.

The reader should pay attention to the following on perusal of this report:

- The report is divided into two major parts:
  - The main report which is divided into numbered chapters.
  - The appendices which are arranged alphabetically.
- Figures, tables and equations are numerated consecutively according to the chapter number. Hence, the first figure in chapter one is named figure 1.1, the second figure figure 1.2 and so on.
- The Harvard method is used for citation. The bibliography can be found after the main report.
- The CD contains internet sources, MatLab scripts and measurements used in this project.

Aalborg University, June 3rd 2009.

Eduardo Fonseca Montero
<edufm@es.aau.dk>

Table of Contents

List of Abbreviations

BEM	Boundary Element Method
BTM	Beam Tracing Method
FDTD	Finite-difference Time-domain
FEM	Finite Element Method
ISM	Image Source Method
MLS	Maximum-length Sequence
PISM	Phase Image Source Method
RIR	Room Impulse Response
RTM	Ray Tracing Method

Chapter 1

Introduction

Computer modelling of room acoustics appeared in the 60s thanks to M.R. Schroeder, and was firstly applied by Krokstad et al. in 1968. Ever since it has been developed to a high extent mainly due to the advent of new improved computer technology. This has enabled accuracy and flexibility in the simulations as well as rapidity in the computation. Hence several applications such as acoustic prediction of existing and nonexisting rooms, electroacoustic prediction or virtual reality has arisen. Moreover the possibility to auralize an acoustic space, i.e. to simulate the listening experience in a room, became an outstanding tool.

Hitherto a number of methods are available for the simulation of the sound field in enclosed spaces by means of a computer. They can be categorized in two major groups. Some methods describe the sound propagation as a wave model approximating the solution of the wave equation, e.g. the finite element method (FEM) or the boundary element method (BEM). These methods are characterized for being very accurate although their usage is in practice restricted to small rooms at low frequencies. In general, they are too computationally demanding to use them routinely for room acoustics prediction.

Another group of methods, based on geometrical acoustics, treat the sound propagation as sound particles moving along ray paths. These techniques such as the ray tracing method (RTM) and the image source method (ISM) are referred to as conventional geometrical acoustic models. They are well suited for high frequencies and are the most widely used for room acoustics prediction.

The conventional geometrical acoustic models describe sound reflections as mere carriers of sound energy. This approach simplifies the calculations required to represent the complex phenomenon of sound reflection. Furthermore, these energy based models usually assume incoherent sound waves and thus neglect the interference phenomenon. Both aforementioned phenomena are related to the phase of the signal.

When applying a conventional geometrical acoustic model for the simulation of small rooms at low frequencies the simulation results may differ from measurements. This is partly due to the fact that the phase information is neglected, being essential for interference phenomenon at this frequency range where room modes appear.

It can also be beneficial to include the phase information in the prediction models when simulating concert hall settings. In this way the accuracy of the prediction can be enhanced and, in addition, it can be used as a mean of obtaining true room impulse responses (RIR) to enable more realistic auralization.

Interference phenomena can only be accounted for if the reflections are modelled as pressure waves with both amplitude and phase. To achieve this, pressure based reflection factors that allow for a phase shift at each reflection must be used, at least in principle. Together with the phase information from the propagation path, a complete phase model is created. In this way it is possible to modify the conventional geometrical acoustic models by including the phase information, thus leading to a *phase* geometrical model for the simulation of room acoustics.

There has been a number of studies focused on the inclusion of phase information into the conventional or energy based geometrical room acoustic models.

Suh and Nelson [1999] included interference into the conventional ISM by accounting for phase changes at reflections by means of plane wave reflection coefficients. The implemented model was validated by comparing simulated impulse responses with measurements carried out in small rooms. The inclusion of complex reflections into the phase image source method (PISM) was shown to increase the accuracy of the predictions. However they also found out that the effect of complex reflections is less significant with low absorptive surfaces.

Lam [2005] also focused on the introduction of phase information into the ISM for the simulation of small rooms. Reflections were modelled by means of plane wave and spherical wave reflection coefficients. It was demonstrated that the latter is able to produce predictions very similar to those provided by the BEM, in the expense of significantly increased complexity. The accuracy of the plane wave coefficient was found to be increasing with frequency and with the rigidity of the materials.

The first attempt of taking into account phase information into the RTM was performed by De Geest and Patzold [1996]. They focused on the simulation of sound fields at low-mid frequencies, comparing the results from their simulations with BEM predictions. Their model was shown to be accurate for rectangular rooms. Conversely, for irregular shaped rooms certain errors were found especially at low frequencies.

Jeong et al. [2008] proposed a further modification of the RTM, namely the beam tracing method (BTM), including phase by means of two types of approximate real reflection coefficients plus the complex wave number. Whereas the angular dependence in the reflection was proved to yield best results, an angle independent reflection coefficient showed reasonably good precision.

Dance et al. [1995] suggested a modified ISM for the calculation of sound pressure in large empty spaces such as laboratories and factories where only the phase change due to the propagation path was considered. Their model was able to approximate interference effects in terms of sound pressure level at certain points, notwithstanding the fact that phase shift on reflection was not taken into account.

Xiangyang et al. [2002] studied the prediction of an enclosed sound field where interference effects exist due to the interaction of multiple sound sources. They demonstrated that the inclusion of phase information into a combination of ISM and RTM is able to predict such a sound field better than the energy tracing method.

Although all the aforementioned studies coincide in the inclusion of phase information as an approach to improve the accuracy of the conventional geometrical acoustic models, the techniques adopted to perform that inclusion differ among the different studies. Several approximations are utilized, depending on a number of factors such as the characteristics of the room and the materials of the surfaces, the frequency range of interest and the ultimate purpose of every investigation.

It is the objective of this thesis to identify the existing techniques of including the phase information into a geometrical acoustic model, as well as implement and evaluate a model able to simulate the sound field including phase in a small room.

The structure of this report is organized as follows. Chapter 2 describes the scope and formulates the goals of the present project. In chapter 3 a brief description of some relevant concepts and equations regarding the reflection of sound against walls is given. Chapter 4 includes a description of the main room acoustics prediction algorithms based on geometrical acoustics, focusing on the ISM. An extension of the conventional ISM in which the phase information is retained, namely the PISM, is described in chapter 5 together with several methods to model the reflection coefficient in order to account for the phase shift on reflection. Chapter 6 concerns the design and implementation of the PISM, explaining the different steps followed in the implementation. In chapter 7, the evaluation of the implemented model is performed by means of a comparison between measured data and simulation results, which are eventually discussed. Chapter 8 presents the conclusions of the project.

Chapter 2

Project Description

This chapter describes the scope and formulates the goals of the present project.

2.1 Scope of the Project

The scope of the project concerns the study and implementation of a model for the simulation of the sound field in rooms. The model is based on a further development of the well known ISM that accounts for the phase information in the prediction, namely the PISM.

The implemented model is used to simulate the sound field in the standard listening room at the facilities of the Section of Acoustics in Aalborg University. The performance of the implemented model is assessed by comparing the simulation results with measurements carried out in the aforementioned room.

2.2 Goals of the Project

The goals of this project are

- to identify the different methods available of including phase information into geometrical acoustic models,
- to implement a model able to simulate the sound field in rooms, accounting for the phase information, and
- to assess the performance of the implemented model.

This leads to the following questions:

- What are the different methods available for including phase information into geometrical acoustic models?
- What are the implications inherent in the procedure of including the phase information?

- Is the PISM able to provide accurate predictions of the sound field in a room?
- If so, under which circumstances is the performance of the model more appropriate?

Chapter 3

Some Concepts on Sound Reflection

In this chapter a brief description of some concepts and equations concerning the reflection of sound against walls is given. They are to be utilized for the development of the project.

3.1 Reflection Factor

When a wave hits a wall, the incident sound is split into different parts. Part of the sound energy will be reflected from the wall, whereas the remaining part will be absorbed by it (either by dissipation in the wall or by transmission through it). Regarding the reflected part, it comes back to the room in the form of a reflected wave originated in the wall. The amplitude and phase of the latter will usually differ from those of the incident wave.

The aforementioned changes of amplitude and phase caused during the reflection of the wave are given by the complex reflection factor R, expressed by equation 3.1 [Kuttruff, 1991]

$$R = |R|\, e^{j\chi}. \tag{3.1}$$

Both the amplitude $|R|$ and phase χ of the reflection factor are frequency dependent. Furthermore, they also depend on the angle of incidence† of the sound wave. The reflection factor, also called reflection coefficient, is a parameter of the wall surface that characterizes its acoustical properties.

The part of sound energy that is being absorbed in the wall corresponds to the fraction $1 - |R|^2$ of the incident energy. Thus the absorption coefficient α of the wall is defined by equation 3.2 [Kuttruff, 1991]

$$\alpha = 1 - |R|^2 . \tag{3.2}$$

In theory, both values $|R|$ and α range from 0 to 1. A wall with no reflectivity presents an absorption coefficient of 1, and hence the wall is said to be totally absorptive.

On the contrary, if there is no sound absorption from the wall ($\alpha = 0$), two cases can occur. If $R = 1$ (in phase reflection, $\chi = 0$), the wall is said to be acoustically hard

†The angle of incidence is defined as the angle formed by the wall normal and the direction of propagation of the incident wave.

or rigid. For the case where $R = -1$ (phase reversal, $\chi = \pi$), the wall is referred to as acoustically soft. Nevertheless, it should be noted that the latter rarely takes place in room acoustics and solely for limited frequency ranges [Kuttruff, 2000].

3.2 Acoustic Impedance

The acoustic impedance Z of a wall is defined as the ratio of the sound pressure p at the surface and the particle velocity v_n normal to the wall, being the latter generated by the aforementioned sound pressure. It is given by equation 3.3 [Kuttruff, 1991]

$$Z = \left(\frac{p}{v_n}\right). \tag{3.3}$$

This quantity describes some of the physical behaviours of the wall and it is more related to its construction than the reflection factor. As the latter, Z is usually complex and depends on the frequency and also on the angle of sound incidence.

The phase angle μ of the acoustic impedance is given by equation 3.4 [Kuttruff, 2000]

$$\mu = \arg(Z) = \arctan\left(\frac{ImZ}{ReZ}\right). \tag{3.4}$$

Measurement of the acoustic impedance is briefly discussed in appendix A. It is commonly found in the literature that the acoustic impedance of a wall is normalized by the characteristic impedance of air $\rho_0 c$, denoting the resulting quantity as the specific acoustic impedance ξ given by expression 3.5 [Kuttruff, 2000]

$$\xi = \left(\frac{Z}{\rho_0 c}\right) \tag{3.5}$$

where $\rho_0 c$ has the value of 415 $Pa \cdot s/m$[†].

The inverse of the acoustic impedance is also used in the literature and it is denoted as the acoustic admittance β. Likewise, the inverse of the specific acoustic impedance is called the specific acoustic admittance of the wall.

3.3 Locally Reacting Surfaces

Locally reacting surfaces are those presenting the property that their acoustic impedance is independent on the angle of incidence of the incoming sound. This phenomenon occurs

[†]For air at a temperature of 20 °C and atmospheric pressure, being the density of air $\rho_0 = 1.21\ kg/m^3$ and the speed of sound $c = 343\ m/s$.

when the particle velocity normal to the surface depends only on the sound pressure of the surface element under consideration and not on that of the neighbouring elements.

In practice, a locally reacting wall is that which does not allow waves to propagate in a direction parallel to its surface. This requirement must also be met by the space behind the wall, if applicable.

For instance, a panel whose adjacent elements are coupled by means of bending forces is not a locally reacting surface. Neither it is a porous layer presenting an air gap between itself and a rigid rear wall. Nevertheless, local reaction can be somewhat maintained in the latter case by using rigid partitions placed in any lateral direction within the air gap. In this way, the wave propagation parallel to the surface can be prevented to some extent.

The concept of locally reacting surface becomes important because when surfaces do not react locally, the simple dependence of the reflection factor or of the absorption coefficient with the angle of incidence given by equations 3.9 and 3.10 is no longer applicable. In this case, there exists a bending wave propagating along the surface that depends on a number of factors such as the kind of mounting where the surface is and the interaction with the air volume behind the surface. The structure of such waves affects the absorption coefficient of the surface (or of the entire arrangement) at oblique incidence, leading to much more complicated relations.

For the development of this report it is assumed that all the acoustic materials are locally reacting.

3.4 Sound Reflection at Normal Incidence

Assuming the direction of the impinging sound to be normal to the wall, it can be demonstrated that the wall acoustic impedance Z for normal incidence is given by expression 3.6 [Kuttruff, 2000]

$$Z = \rho_0 c \frac{1+R}{1-R} \tag{3.6}$$

and if the acoustic impedance is known, the reflection factor R can be found be rewriting equation 3.6 as follows

$$R = \frac{Z - \rho_0 c}{Z + \rho_0 c} = \frac{\xi - 1}{\xi + 1}. \tag{3.7}$$

From expression 3.6 the following can be established. For the case of $R = 1$ (rigid wall), the acoustic impedance becomes $Z = \infty$. On the contrary, if $R = -1$ (soft wall), the acoustic impedance vanishes. For the case of $R = 0$ (totally absorptive wall), the acoustic impedance equals the characteristic impedance of air, i.e. complete matching of the wall to the medium. The latter case is the only one where there is no reflection whatsoever from the wall. It is equivalent to an open window in a room through which the sound goes away.

3.5 Sound Reflection at Oblique Incidence

Considering now the incident sound as coming from any possible angle of incidence θ, it can be shown that the wall acoustic impedance Z for oblique incidence is given by the expression 3.8 [Kuttruff, 2000]

$$Z = \frac{\rho_0 c}{\cos\theta}\frac{1+R}{1-R}. \tag{3.8}$$

When having knowledge of the acoustic impedance, the reflection factor R can be found by rearranging equation 3.8, leading to equation 3.9

$$R = \frac{Z\cos\theta - \rho_0 c}{Z\cos\theta + \rho_0 c} = \frac{\xi\cos\theta - 1}{\xi\cos\theta + 1}. \tag{3.9}$$

Inserting equation 3.9 in equation 3.2 results in the absorption coefficient for oblique incidence, given by expression 3.10

$$\alpha(\theta) = \frac{4\Re(\xi)\cos\theta}{(|\xi|\cos\theta)^2 + 2\Re(\xi)\cos\theta + 1}. \tag{3.10}$$

3.6 Sound Reflection at Random Incidence

The absorption coefficient for random incidence α_{ran} is given by the so-called Paris' formula, according to expression 3.11 [Kuttruff, 2000]

$$\alpha_{ran} = \int_0^{\pi/2} \alpha(\theta)\sin(2\theta)d\theta. \tag{3.11}$$

If the surface under consideration reacts locally, it is possible to model the angular dependence of the absorption coefficient by equation 3.10. Introducing the latter in 3.11 and computing the integral yields an expression for the random incidence absorption coefficient as a function of the absolute value and the phase angle of the specific acoustic impedance.

3.7 Diffusion

The concept of diffuse reflection consists of the fact that when a sound ray or wave hits a surface, part of the reflected sound follows a specular behaviour (angle of incidence equals angle of reflection) whereas the rest of the reflected sound is reflected in other directions, i.e. following a diffuse fashion [Svensson and Kristiansen, 2002]. Diffuse reflections can be caused by surface roughness and/or discontinuities of the surface impedance and hence the directivity of the diffusely reflected sound depends on those factors.

3.8 Diffraction

The concept of diffraction is related with the capacity of sound waves to bend around corners and obstacles and to be extended after passing through small openings. Diffraction is a typical wave phenomenon and in room acoustics can occur in several scenarios [Vorländer, 2008]: due to obstacles with free edges in the room space, at corners and edges in the room, or at boundaries between materials with different impedances and hence absorption.

Chapter 4

Computer Modelling of Room Acoustics

In this chapter a description of the main room acoustics prediction algorithms based on geometrical acoustics, namely the RTM and the ISM, is included. Whereas the description of the RTM is a brief introduction to the principle of the method, the ISM is further explained since it is the basis of the present work. As well, a comparative of the aforementioned methods is included.

Computer modelling of room acoustics appeared in the 60s thanks to M.R. Schroeder, and was firstly applied by Krokstad et al. in 1968. Ever since, it has been developed to a high extent and consequently it has taken over the room acoustics simulation role against traditional scale models. It became more accurate, more flexible and user-friendly, and also cheaper than scale models.

The room acoustic prediction methods or, in other words, the modelling of the sound propagation from a source to a receiver within a room can be classified according to figure 4.1.

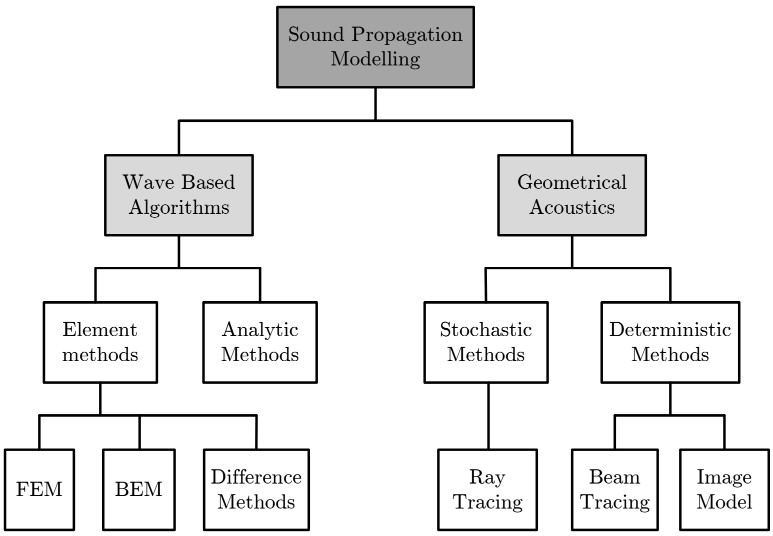

Figure 4.1: Classification of methods for simulating sound propagation in rooms. Partially taken from [Vorländer, 2008].

One possibility is to describe the sound propagation by a wave model, leading to numerical methods that approximate the solution of the wave equation [Rindel, 2000]. Some of these numerical methods are the FEM, the BEM and finite-difference time-domain (FDTD) method. These methods are based on a division of the space or surfaces into small elements or nodes, and are proved to provide very accurate predictions but restricted to cases of small rooms and low frequencies [Kleiner et al., 1993].

Another possibility is to describe the sound propagation by sound particles moving along rays. This approach, based on geometrical acoustics, is suitable for sound at high frequencies. There are two conventional geometrical methods namely the ISM and the RTM for the simulation of sound in rooms. Most simulation commercial software use either one of them, or a combination of the best features of both, yielding the so-called hybrid methods [Rindel, 2000].

It should be noted that the list of algorithms shown in figure 4.1 is not in any way complete since more prediction methods can be found in the literature, mainly some that have been developed recently. The numerical methods will not be further treated since they are considered out of the scope of the project. In the following, the basis of the geometrical acoustic models is presented.

4.1 Geometrical Acoustics

Geometrical acoustics can be understood by using the analogy of geometrical optics. The simplification made here consists of assuming vanishingly small wavelengths, which take place in the high frequency range. This assumption is valid provided the dimensions of the room under consideration and its walls are large compared with the wavelengths of sound involved.

Once done this assumption, the concept of sound wave can be replaced by that of a sound ray, which can be defined as an energy carrier representing *a small portion of a spherical wave with vanishing aperture which originates from a certain point* [Kuttruff, 2000]. It should be noted that the concept of a sound ray is an idealisation as well as the concept of a plane wave.

A sound ray is thus a straight line perpendicular to a quasi-plane wave carrying sound energy, i.e. the energy that in the real world is transported by a sound wave can be addressed here to a particle travelling along a sound ray. Then, the amount of rays hitting a receiver determines the amount of energy received.

Sound rays present a direction of propagation, and are subject to the same laws of propagation as light rays, except for the velocity. Thus the energy carried by a sound ray would remain constant if the medium were lossless. Nevertheless the intensity of a sound ray decreases with $1/r^2$ where r denotes the distance from its origin. Whereas reflection of sound rays does occur in geometrical acoustics, either in specular or diffuse manner, typical wave phenomena such as diffraction are neglected at least in principle[†] since propagation on straight lines is the main rule. Likewise interference phenomena are in principle ignored. This means that the superposition of two rays is performed solely in terms of addition of their energy or intensity, whereas their mutual phase relations are not taken into account.

Given the propagation of rays, impulse responses containing appropriately delayed and weighted Dirac pulses can be constructed.

To sum up, geometrical acoustics describes only a partial aspect of the acoustical phenomena occurring in a room, although of great importance. The representation of the sound field is limited to energy, transition time and direction of rays. As a rule of thumb, this approach is sufficiently accurate in large rooms for the frequency region above the Schroeder frequency.

The algorithms of the most common commercial software for room acoustic prediction are based on geometrical acoustics, and their performance has been evaluated by means of intercomparison tests namely round-robin tests [Bork, 2005a][Bork, 2005b] where their efficiency and limitations have been compared.

In the remainder of this chapter the major methods within geometrical acoustics are identified, their principles are explained and their main features are commented. Two methods can be distinguished: one based on ray tracing and another based on image sources. Both present different physical approaches and have opposite advantages and drawbacks. By combining the best features of each the so-called hybrid methods are created.

4.2 RTM

The principle of the RTM is depicted in figure 4.2. A sound source S is located at a certain position within a room and it radiates sound in all directions. The radiation of sound can be seen as an emission of sound particles at a certain moment $t = 0$. Each sound particle carries a certain energy and travels at sound velocity on a straight path until it hits a wall. Walls are assumed to be plane for simplicity. The particle can be reflected either specularly or diffusely. In the former case, the new direction is calculated according to the law of geometrical reflections. For the latter case, two random numbers are generated from which both the azimuth and the polar angle of the new direction are computed [Kuttruff, 2000]. The latter is the angle between the diffused particle path and the wall normal and it is distributed following the so-called Lambert's cosine law. After its reflection, the particle follows the new direction towards the next wall, and so on.

There are two alternative approaches for the algorithm depending on the way in which wall absorption is taken into account [Vorländer, 1989]. It can be accounted for by

[†] There exist however some recent works such as [Pulkki et al., 2002] in which an attempt to account for the effect of diffraction within geometrical acoustic models is studied.

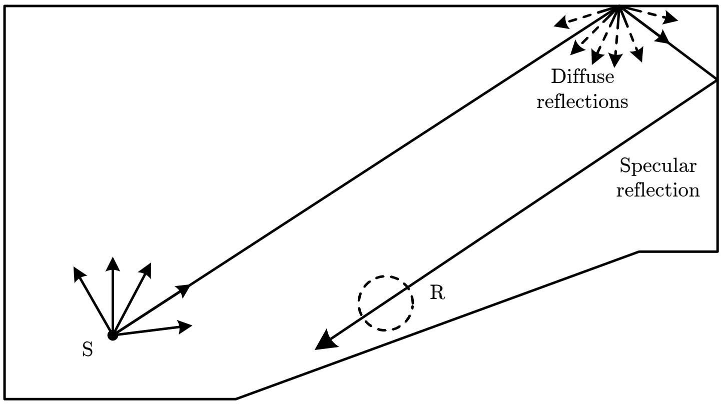

Figure 4.2: Principle of ray tracing over the elevation view of a room. S is the source. R is the receiver, also called counter [Kuttruff, 2000].

reducing the energy of the particle by a factor $1 - \alpha^{\dagger}$ whenever a reflection occurs, i.e. a multiplicative reduction of the particle energy. Or it can be accounted for by generating a random number which is to decide whether the particle proceeds along or is absorbed, i.e. the so-called controlled particle annihilation. The effect of air attenuation can also be considered in a similar way. Once the energy of the particle is below a predefined value or the particle has been absorbed, the path of a new particle is traced. This procedure is repeated until all particles that have to be emitted by the source at the moment $t = 0$ have been followed up [Kuttruff, 2000].

In order to compute the results, energy and arrival time of each particle are registered whenever a particle arrives at a predefined detector, also called counter (R in figure 4.2). If needed, also the direction from which it has arrived. The detectors are typically plane areas or spherical volumes [Kuttruff, 1993]. After tracing the paths for all particles and classifying the gathered data, the energies corresponding to all particles received are added within determined time intervals. The result of this process is a histogram showing the temporal distribution of the energy received. Therefore it can be considered as a short-time averaged energetic impulse response [Kuttruff, 2000], i.e. an approximation to the energetic impulse response of the enclosure.

The degree of the approximation depends on the time resolution achieved as well as the number of particles involved in the procedure. Regarding the former, the selection of the time intervals of the histogram is critical. Long intervals lead to a crude approximation of the true impulse response since details are lost by averaging. On the other hand, short intervals may yield random fluctuations superimposed on the results.

With respect to the number of particles, the accuracy of the results is conditioned by the amount of particles counted by the detector. Two facts can be derived from this dependency. Firstly, the detector must be defined so that it is not too small. Secondly,

†Where α is the absorption coefficient of the wall.

the total number of particles emitted by the source must be sufficiently large. As a rule of thumb, Kuttruff [2000] suggests the usage of $10^5 - 10^6$ sound particles for detector dimensions of the order of 1 m.

The advantages of the RTM are that it can handle diffuse reflections and that it can be applied to model the effect of curved surfaces. Regarding the computation time, it increases only proportionally with the length of the impulse response [Vorländer, 1989]. On the other hand, as outlined above, the temporal resolution is limited.

Numerous refinements of the described algorithm has been presented up to date. Some are based on an improved definition of the detector. Furthermore, replacement of rays by beams, e.g. triangular or conical, leading to the BTM has yield interesting improvements in the accuracy of the results. Nevertheless it also present other drawbacks and computational difficulties (see [Dalenbäck, 1996]).

4.3 ISM

The method of image sources is very old but however its practical application started only with the advent of digital computer. Allen and Berkley [1979] proposed in 1979 an efficient and simple algorithm of the ISM restricted to a rectangular enclosure. Afterwards, Borish [1984] presented in 1984 a generalized algorithm extended to any arbitrary geometry. Ever since numerous works have taken care of improving the accuracy, efficiency and flexibility of the method up to date.

Let us begin explaining the concept of image source. When a sound ray strikes a surface it is usually reflected from it. Let us assume it does it with a specular behaviour, according to the reflection law from optics. Let us also assume the boundaries considered are composed of plane and uniform surfaces. Hence the reflected ray remains in the plane determined by the impinging ray and the normal to the surface under consideration. Furthermore the angle between the normal and the reflected ray equals that between the normal and the impinging ray.

When the conditions above are given, it is possible to take advantage of the concept of image sources for the construction of sound paths. An example of this is illustrated in figure 4.3, where a sound source A is located in front of a wall. It is feasible to think of every ray reflected from the wall as being originated from a virtual or image source[†] A', positioned at the other side of the wall. A' is located on the line perpendicular to the wall, at the same distance from the latter as the original source A. It can be said that to create the image source A' one has to *mirror* the original source with respect to the wall.

Now the effect of the wall can be disregarded since it is accounted for by that of the image source. The image source emits simultaneously the same signal as the original source, and its directional behaviour is symmetrical.

[†]Both terms virtual source and image source can be found in the literature. In the present work the latter is used henceforth.

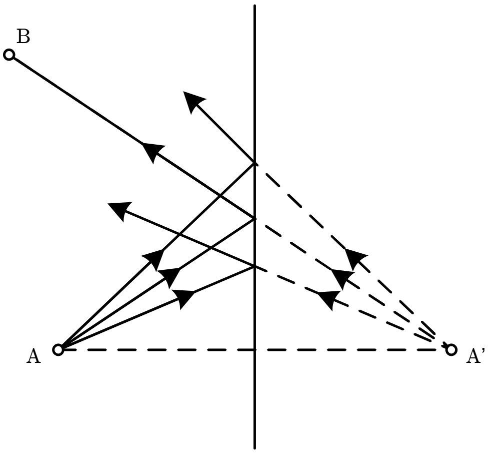

Figure 4.3: Construction of an image source [Kuttruff, 2000].

Usually not all the energy incident on the surface is reflected. The fraction of sound energy that is not reflected is given by the absorption coefficient α. It usually depends on the angle of incidence and the frequencies present in the incident sound. Therefore the reflected ray has generally lower energy than the incident ray, by a fraction $1 - \alpha$, and different spectral content.

Let us suppose now a sound ray emitted from a sound source positioned within a closed room. In this case, the ray is reflected not once but several times from walls, ceiling and floor. This sequence of reflections continues until the energy carried by the ray vanishes, due to the fact that part of it is lost in every reflection. This more complicated sound path can be constructed by extending the concept of image sources, leading to image sources of higher order. In first place, the first-order image sources with respect to all walls are calculated. From each of these, second-order image sources are created proceeding the same way with respect to all walls except that by which the first-order image source was mirrored last. This procedure is repeated until a previously defined order of image sources is reached. For instance, a fourth order image source represents a ray that has undergone four wall reflections.

A simplified example of the aforementioned process for a second-order reflection can be seen in figure 4.4, where a sound ray emitted by the original source A is represented. At some point it strikes a wall, and from that moment on it continues as being originated from the first-order image source A' until it hits a second wall. Then, the path of the ray is determined as if it came from the second-order image source A". The first-order image source A' is created my mirroring the original source with respect to the wall where the first reflection takes place. Likewise the second-order image source A" is created by mirroring the first-order image source A' with respect to the wall where the second reflection occurs.

Depending on the geometry of the room, the pattern of points given by the constellation

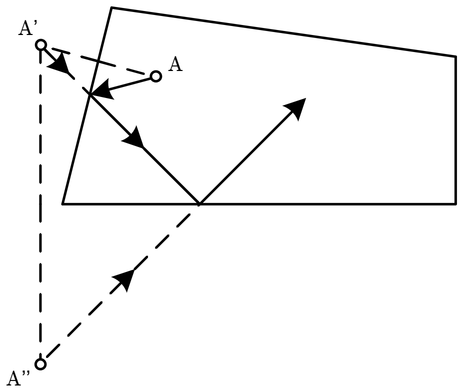

Figure 4.4: Image sources of first and second order [Kuttruff, 2000].

of image sources may differ considerably. For complex rooms with a great number of walls, the pattern may be very complicated. Contrarily, for enclosures with high regularity, the pattern of image sources presents as well certain regularity. The simplest case is given for the rectangular room, also denoted shoebox shaped. In this case certain image sources of the same order are complementary and coincide, yielding a regular pattern as that of figure 4.5.

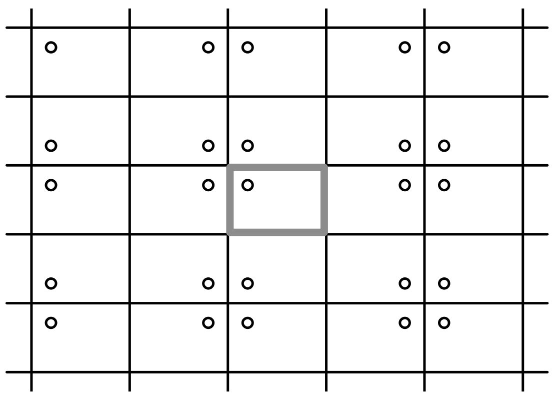

Figure 4.5: Pattern of image sources for a rectangular room. The accentuated box in the centre depicts the original room. Surrounding it are the image rooms, each containing one image source [Borish, 1984].

The accentuated room in figure 4.5 represents the original room. Each of the four image rooms adjacent to the walls of the original room contain one first-order image source. Hence those rooms adjacent to the corners of the original room contain in turn second-order image sources, and so on. The lattice of points depicted in figure 4.5 must be completed in the direction perpendicular to the drawing plane. Because of the regularity of this pattern, the location of the image sources can be calculated in an easier way. On the other hand, for irregular shapes such a task becomes more tedious.

An issue inherent in the ISM that should be addressed is the visibility of the image sources. Depending on the geometry of the room, it may be that certain image sources do not contribute to the response at a given receiver position. Such image sources are denoted *invisible* from the receiver under consideration. This problem was studied first by Borish [1984] and subsequently by Vorländer [1989].

For the example given in previous figure 4.5, all image sources are visible. This is so due to the fact that all image rooms fill up the entire space with no overlap among them and without leaving uncovered regions [Kuttruff, 2000]. On the contrary, irregular shaped rooms yield much more irregular patterns of image sources where image rooms overlap each other in different manners. For these cases, the visibility of every image source for a given receiver position must be checked. In fact it turns out that most of higher order image sources are invalid.

The matter of finding an invisible image source by means of the so-called visibility test is illustrated in figure 4.6, for a second-order image source.

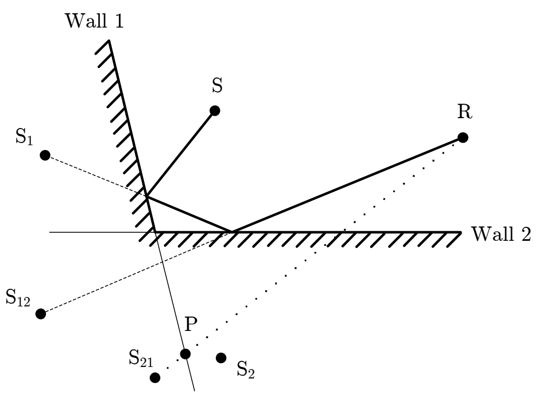

Figure 4.6: Geometrical backtracing of sound paths from receiver R to the original sound source S. Image source S_{12} is visible. S_{21} is not visible since the intersection of the dotted line RS_{21} with wall 1 is not located within the real boundaries of the latter [Vorländer, 1989].

Figure 4.6 shows a source S and a receiver R within a room. The manner to check the visibility of S_{12} is as follows. The index of the latter indicates that wall 2 was involved last in the sound path. S_{12} is a visible image source since the line connecting it with R does intersect the wall 2 within the extension of the actual wall. Next, the procedure is repeated considering the intersection point as receiver, and aiming at the previous image source in the chain (S_1 in this case). This technique is repeated until the original source is reached. If one of the computed intersection points is not within the real wall boundaries (as the case of the dotted line RS_{21}, which intersects wall 1 in the point P, out of its boundaries), the image source is considered not visible and thus omitted.

The procedure of the visibility test as described above, i.e. backtracing the paths from the receiver to the original source, turns out to be very computation demanding, to the extent of being impractical for complex shaped rooms due to the huge computation time required.

The computation time of the ISM is mainly dependent on the maximum order of image sources. Let us assume a room composed of n_w walls. Every wall is associated with one first-order image source. Each of those first-order image sources is to be mirrored by all walls except one yielding $n_w(n_w - 1)$ new second-order images. By repeating this procedure it can be found that the number of image sources up to the reflection order i_0 in a room with n_w walls increases exponentially with i_0, as given by expression 4.1 [Vorländer, 1989]

$$N_{IS} = \sum_{k=0}^{i_0-1} n_w(n_w - 1)^k = \frac{n_w}{n_w - 2}\left[(n_w - 1)^{i_0} - 1\right]. \tag{4.1}$$

In light of expression 4.1, it can be noticed that the number of image sources grows rapidly with increasing distances from the original source, i.e. with the length of the impulse response to be computed.

The large amount of image sources required can be demonstrated through an example given in [Kuttruff, 2000]. The example considers a 12000 m^3 room, made up of six walls in a non rectangular shape, with an area of 3600 m^2. It can be derived that for this particular case a sound particle undergoes 25.5 reflections per second on average†. Thus to compute an impulse response of 400 ms, image sources up to order $i_0 = 10$ are required at least. Introducing order and number of walls into equation 4.1 yields a number of image sources to be constructed of around $1.46 \cdot 10^7$. Without going into details, it is possible to foresee that the amount of calculations needed to perform the visibility test as previously described is vast due to the large amount of image sources to process. Hence, depending on the room geometry it may not be possible to reach an acceptable computation time.

Furthermore it must be noted that the number of image sources that turns out to be valid after the visibility test is extremely low, so that most of calculations are in vain. If the considered example were shoebox shaped there would be only 1560 image sources (all of them visible), according to expression 4.2‡ [Kuttruff, 2000]

$$N_{ISr} = \frac{2}{3}(2i_0^3 + 3i_0^2 + 4i_0). \tag{4.2}$$

Fortunately, an improved method to carry out the visibility test was proposed by Vorländer [1989]. In this case the separation between the visible image sources from the invisible ones is done by ray tracing. Firstly a specular ray tracing process is performed, noting the index of all those walls involved in the reflection of every detected particle. Then the

†The average of reflections per second is given by $cS/4V$, c being the sound speed, S the total wall area and V the room volume [Kuttruff, 2000].

‡It should be noted that equation 4.2 is written incorrectly in [Kuttruff, 2000]. The expression included in the present work is the correct version, provided by the author of [Kuttruff, 2000] by private communication.

position of the visible image sources can be computed based on that list. The only problem is that ISM supposes a point receiver whereas RTM assumes a finite extension of the counter. Hence in the visible image sources list there will be some wrong sources. One can either neglect this effect, which depends on the counter volume or, to overcome this problem, the conventional test namely backtracing of the paths from receiver to original source can be performed.

The procedure suggested by Vorländer is found to provide gain of computing speed with respect to the conventional visibility test, mainly when high order image sources come into play [Vorländer, 1989] and it has been utilized in several works, e.g. [Suh and Nelson, 1999]. Nowadays several variants of this approach are used, based on cone tracing or pyramid tracing.

Thus it can be concluded that as the room deviates from the shoebox geometry and the number of walls increases, finding the location of the image sources becomes a more difficult process. Furthermore, in this case not all the image sources are visible and therefore a visibility check must be carried out.

Once all valid or visible image sources are determined, the original room is no longer needed. The sound signal received at a certain point is the superposition of the contributions of all image sources plus the original one. All of them emit simultaneously the same signal.

Hence the energy impulse response can be computed by adding contributions of all image sources assuming the original source produces a short impulse represented by a Dirac function $\delta(t)$. To compute the energy impulse response at a receiver, the arrival time and the level or strength of every contribution must be calculated. The arrival time of every sound ray is determined by the distance from the receiver to its corresponding image source.

The level of a particular contribution depends mainly on the absorption coefficient of the walls involved in its particular sound path, i.e. those crossed by the straight line connecting image source and receiver. It must be noted that the level of every contribution depends also on the direction of radiation, if the original source is directional, and the source output power. Moreover, it is affected by spherical radiation and air attenuation.

Therefore the contribution of a particular image source to the energy impulse response is given by equation 4.3 [Kuttruff, 2000]

$$\frac{P}{4\pi c r^2}\rho_{m_1}\rho_{m_2}\dots\rho_{m_i}\delta\left(t-\frac{r}{c}\right), \tag{4.3}$$

where P is the power radiated by the original source, r is the distance between the image source under consideration and the receiver, $\rho_k = 1-\alpha_k$ denote the reflection coefficients of the walls $m_1, m_2, \dots m_i$ involved in the particular sound path and c is the speed of sound. The energy arrival time is determined by the factor r/c. It can be seen how the contribution from an image source represented by equation 4.3 accounts for the walls absorption and the $1/r^2$ law due to spherical radiation, i.e. the sound energy is inversely proportional to the distance squared. However no air attenuation is included in equation 4.3. In the real world, waves are also attenuated by absorption in the medium. This effect can be taken into account by means of the attenuation factor m_a that can be determined according to expression 4.4 [Kinsler et al., 2000]

$$m_a = 5.5 \cdot 10^{-4}(50/h)(f/1000)^{1.7}, \tag{4.4}$$

where h denotes relative humidities in percent between 20 and 70 and f denotes frequencies within the range 1.5 to 10 kHz.

To account for air attenuation the energy amplitude must be reduced by the exponential term $\exp(-m_a r)$ [Kuttruff, 2000]. Hence this factor is to multiply equation 4.3.

4.3.1 Limitations and Considerations

Unavoidable error is that given by necessary truncation of the amount of image sources at a certain order [Vorländer, 2008]. The computation time increases exponentially with the length of the impulse response and hence the ISM presents, in its conventional form, a large limitation when it comes to efficiency. It should be stressed that there is no statistical error inherent in this algorithm, i.e. it is very accurate, and the time resolution provided is very high which becomes important for auralization tasks for instance.

One drawback of the ISM is that it is restricted to specular reflections [Kuttruff, 1993], i.e. it cannot handle diffuse reflections. This fact has proven to be one of the most important limitations of the algorithm due to the fact that pure specular modelling creates a rough approximation of the physical sound field in most of the rooms.

One interesting feature of the ISM is that the receiver can be mirrored instead of the source, leading to a lattice of image receivers. This can be advantageous for instance when the source is moving while the receiver is fixed.

In light of the description above, it can be stated that this algorithm in its classical form (Allen and Berkley/Borish) is applicable and efficient for the following cases [Vorländer, 2008]:

- for short impulse responses,
- for rooms with simple geometries, i.e. small number of walls n_w, and
- for rectangular rooms, since the visibility test can be omitted.

4.4 RTM vs. ISM

Both RTM and ISM follow different physical approaches. The main difference between them consists of the procedure for the energy detection and the nature of physical energy propagation [Vorländer, 2008]. Table 4.1 shows their main features.

Algorithm	Category	Energy spreading by distance	Energy detectors
RTM	Stochastic	Stochastic by counting	Volumes
ISM	Deterministic	Deterministic by distance	Points

Table 4.1: Basic algorithms of room acoustics computer simulations [Vorländer, 2008].

As well, both algorithms differ in the following issues.

Accuracy

RTM outcomes represent temporal energy distributions with poor resolution rather than true impulse responses, while the ISM provides high resolution responses. Apart from that, all reflections found by the RTM will match those found by the ISM but the latter will also find a number of reflections that the RTM missed. Borish [1984] stated that even though it is possible to refine the RTM so that it provides more accurate information, the ISM provides the desired information as a matter of course.

Reflection Handling

ISM is restricted to specular reflections whereas RTM handles diffuse reflection.

Computation Time

ISM computation time increases exponentially with the desired length of the impulse response. RTM computation time is proportional to the impulse response length.

Algorithm

When considering the frequency dependence of wall absorption in the ISM, different power outputs are to be attributed to the image sources according to the effect of the wall reflections they represent. In this case, the lattice of image sources remains the same for all frequencies.

In contrast, the stochastic nature of the RTM including diffusion requires one pass per frequency band, i.e. for every set of absorption and scattering coefficients. That is because the diffusion provided by a surface is frequency dependent.

Psychoacoustics

According to Kuttruff [1993], *when applied to the total room impulse response, the image source method yields much more information on sound transmission than is significant from a psychoacoustical point of view.*

4.5 Hybrid Methods

It has been shown how the RTM and the ISM have opposite advantages and weaknesses. For this reason it is worth combining the best characteristics of each yielding the so-called hybrid methods. These methods feature diffuse reflections and provide a fine temporal resolution. Normally, they use the ISM for the early part of the impulse response, employing a specular ray tracing process (or variation thereof) for the calculation of the visible image sources. Moreover the later part of the impulse response is handled by the RTM, in one if its various versions, since diffuse energy dominates the reverberation process after a few reflections [Vorländer, 2008].

Hybrid methods are apparently the key to the modelling of impulse responses that resemble measured data to a great extent. For that reason, most of well-known commercial software solutions, such as CATT-acoustic [CATT, 2002] and ODEON [Christensen, 2008], make use of this type of algorithms.

Chapter 5

Inclusion of Phase into the ISM

In this chapter an extension of the conventional ISM in which the phase information is retained, namely the PISM, is described. Furthermore, several methods to model the reflection coefficient in order to account for the phase shift due to the reflection of sound are presented.

5.1 PISM

The PISM is somewhat different from the conventional ISM described in section 4.3, notwithstanding the fact that the physical principle is the same. Both are based on contributions from image sources added together for the construction of the response at a certain receiver.

In the conventional ISM, energy impulse responses are constructed from the energy variation as a function of time of arrival. In a similar fashion, pressure impulse responses can be obtained by the PISM, in which the pressure at each time is calculated.

The total sound pressure at a certain receiver can be modelled by adding complex spherical wave contributions from the original source and the image sources. Thus the total complex sound pressure is given by equation 5.1 [Suh and Nelson, 1999]

$$p(w) = \frac{\rho_0 q(w) e^{-jkr_0}}{4\pi r_0} + \sum_{n=1}^{N_{IS}} p_n(w). \tag{5.1}$$

The first term of equation 5.1 represents the direct sound, coming from the original source, where $q(w)$ is the source strength, k the wave number and r_0 the distance from the original source to the receiver. It has been shown in [Jeong et al., 2008] that the wave number k of equation 5.1 can be substituted by the complex wave number $\tilde{k}$ if the attenuation due to air absorption is to be accounted for. The complex wave number $\tilde{k}$ is expressed by equation 5.2

$$\tilde{k} = k - jm_a/2 \tag{5.2}$$

being m_a the attenuation factor due to air absorption given in equation 4.4.

The second term of equation 5.1 represents the contributions from all the considered image sources. Each of those contributions can be expressed by equation 5.3 [Suh and Nelson, 1999]

$$p_n(w) = \frac{\rho_0 R_1(w) R_2(w) \ldots R_i(w)}{4\pi r_n} q(w) e^{-jkr_n}, \tag{5.3}$$

where $R_k(w)$ denote the reflection coefficients of the walls $1, 2, \ldots i$ involved in the particular sound path and r_n is the distance between the image source under consideration and the receiver.

Since the conventional ISM deals with energy, there are no complex numbers involved. On the contrary, it can be seen in equations 5.1 and 5.3 that there is complex notation in the PISM because the phase information is used to deal with wave interference.

The phase information is included in the PISM by two different means:

- due to the reflection of sound against boundaries and
- due to the sound propagation path.

These two means are represented in equations 5.1 and 5.3. On the one hand the reflection coefficients $R_k(w)$ represent the acoustical properties of the surfaces, in terms of amplitude and phase shift at each reflection. On the other hand the exponential terms account for the phase shift during the propagation.

Section 5.2 presents a number of approaches for modelling the reflection coefficient in order to account for the phase information due to the reflection of sound.

5.2 Methods of Phase Inclusion into Geometrical Acoustic Models

A way to predict the wave nature of room acoustics can be to modify the conventional geometrical acoustic models so as to retain the phase information. The idea is to model the complex sound pressure reflection phenomenon by including a pressure wave based reflection coefficient in the conventional geometrical model, instead of the simple energy absorption. Together with the phase information from the propagation path, a full phase model can be obtained. A number of approaches found in the literature for modelling the reflection coefficient are described next:

5.2.1 Plane Wave Reflection Coefficient

Sound rays present in a geometrical acoustic model can be considered as a representation of the propagation of plane waves. Therefore it is possible to model the reflection of such waves at surfaces by means of plane wave reflection coefficient R. It was already included in chapter 3 and it is here again for completeness, given by equation 5.4

$$R = \frac{\xi \cos\theta - 1}{\xi \cos\theta + 1}, \tag{5.4}$$

which is a function of the angle of incidence θ measured from the normal, and the specific acoustic impedance ξ of the surface with which the wave is reflected.

Several previous works have used the plane wave reflection coefficient approach in its different forms, which are described in the following.

Complex Reflection Coefficient

The plane wave reflection coefficient can of course be implemented by its original form, i.e. a complex reflection coefficient which is angle and frequency dependent, given by equation 5.4

To perform this raw implementation of the reflection coefficient it is required to measure the complex impedance of the materials involved. In [Suh and Nelson, 1999] this coefficient is utilized, but only for those surfaces which present high absorption, e.g. plastic foam, carpet and insulation board. The normal specific acoustic impedance was measured by an impedance tube test with rigid-backing condition, which yields the resistance and reactance composing the complex expression of the impedance. Thus a complex reflection coefficient is obtained.

However instead of dealing with complex reflection coefficients, another strategy can be to approximate that value. Different approximations have been found are described next.

Angle Independent Real-valued Reflection Coefficient

Some previous works approximate the complex reflection coefficient by an angle independent, real-valued reflection coefficient.

The real part of the normal reflection coefficient is calculated based on the random incidence absorption coefficient α_{ran} of the surface, according to expression 5.5

$$R_r = \sqrt{1 - \alpha_{ran}}. \tag{5.5}$$

The imaginary part of the reflection coefficient is assumed to be zero for acoustically hard walls, e.g. concrete and plaster. Thus the only input for this method is the random incidence absorption coefficient which in [Suh and Nelson, 1999] was assumed to be constant in frequency and whose values were arbitrarily set for every material. In principle, this approximation yields small error for this sort of walls. This approach assumes in phase reflections.

Furthermore, Jeong et al. [2008] implemented this method allowing a 180 ° phase shift for the reflection depending on the surface features and providing frequency dependent absorption. To accomplish it, the initial expression 5.5 was modified leading to equation 5.6

$$R_r = \pm\sqrt{1-\alpha_{ran}}. \tag{5.6}$$

The positive sign of expression 5.6 is applied for reflections taking place with acoustically hard materials, corresponding thus with equation 5.5. Contrarily, reflections with soft materials are formed with the negative sign, creating an out of phase reflection. Rindel [1993] specifies that the negative sign should be utilized only for materials whose impedance can be considered to be small if compared to $2\rho_0 c$. As well, it is suggested that porous absorbers should be assumed to be soft whereas heavy and dense materials, e.g. concrete and/or wooden panels should be regarded as hard.

Lehmann and Johansson [2008] followed an approach based on using the negative version of equation 5.6 for all surfaces. They stated that it yields higher accuracy when replicating the effects of a real acoustic environment, in terms of computing more realistic RIR shapes.

To realize this method, solely information of the surface absorption is required. No complex impedance values are involved.

Angle Dependent Real-valued Reflection Coefficient

Another possible approximation of the complex reflection coefficient is by means of an angle dependent real-valued reflection coefficient. It was originally proposed by Rindel [1993] and subsequently applied in [Jeong et al., 2008] among others. This coefficient is computed based on an empirical approximation of the surface impedance Z, containing the acoustical properties of the material, and the radiation impedance Z_r, containing influences of both angle of incidence and surface area, as given by equation 5.7

$$R_{r\theta} = \frac{Z - Z_r(\theta)}{Z + Z_r(\theta)}. \tag{5.7}$$

The surface impedance Z, which is assumed to be real, can be calculated from the angle independent real-valued reflection coefficient R_r of equation 5.6 and from the so-called equivalent radiation impedance, Z_r^*, by means of expression 5.8

$$Z = Z_r^* \frac{1+R_r}{1-R_r}. \tag{5.8}$$

The equivalent radiation impedance Z_r^* is a compensation factor proposed by Rindel [1993]. It is used to match the random incidence absorption coefficient obtained from the Paris' formula (see equation 3.11) through the proposed coefficient $R_{r\theta}$, with the initially measured random incidence absorption coefficient α_{ran}. This process served as a validation of the proposed approximation†.

Such a validation led to the empirical determination of the equivalent radiation impedance whose final results are included next. For large areas, the normalized value $Z_r^*/\rho_0 c$ should be 2. However for areas similar to 11 m^2‡ a somewhat lower and frequency dependent value is obtained, as given in table 5.1.

Frequency [Hz]	$Z_r^*/\rho_0 c$
125	1.04
250	1.35
500	1.53
1000	1.62
2000	1.64
4000	1.64

Table 5.1: Values of the equivalent radiation impedance corresponding to a test area of 11 m^2 [Rindel, 1993].

Thus expression 5.8 constitutes the first step of the approximation, i.e. a purely real positive impedance value is defined for the surface. This value is equivalent to the true complex surface impedance in such a way that both provide the same absorption coefficient. It should be noted that expression 5.8 is a more elaborated version than that proposed by Suh and Nelson [1999] for the same purpose, where the equivalent radiation impedance is absent.

Regarding the radiation impedance, Z_r, for finite areas it is a complex value. Nevertheless Rindel developed an approximation to its real part consisting of expression 5.9 [Rindel, 1993]

$$Z_r = \rho_0 c \left[\left(\cos^2\theta - A\frac{2\pi}{ke} \right)^2 + B\left(A\frac{2\pi}{ke} \right)^2 + \left(\frac{2\pi}{(ke)^2} \right)^4 \right]^{-1/4}. \tag{5.9}$$

†Should the reader require further information, it can be found in [Rindel, 1993].

‡ISO 354 recommends a sample material of between 10 and 12 m^2 for the measurement of the random incidence absorption coefficient α_{ran}.

In expression 5.9, A and B are empirical constants found to be 0.6 and π respectively by trial and error method, θ is the angle of incidence and the factor ke is a relation where k is the wave number and e denotes the characteristic dimension of the surface expressed as $e = 4S/U$, S being the area and U the perimeter. The results of this approximation deviate from the numerical results within ± 10 % for $ke > 8$ and up to ± 20 % for $ke < 8$.

It is important to note that in this approximation the reflection coefficient computed, and hence the absorption, depends on the size of the surface under consideration through the radiation impedance.

Therefore, using the approximations given by equations 5.8 and 5.9, and introducing them in equation 5.7, an angle dependent real-valued reflection coefficient can be computed for a surface with known α_{ran}. Neither impedance measurements nor complex notation is involved.

Admittance-based Reflection Coefficient

Unlike in the aforementioned cases, Lam [2005] proposed a formulation of the plane wave reflection coefficient based on the admittance instead of the impedance. The expression of this coefficient can be derived from equation 5.4 and is given by equation 5.10

$$R = \frac{\cos\theta - \beta}{\cos\theta + \beta}. \tag{5.10}$$

It is a function of the angle of incidence θ and the surface admittance β. Several implementations of this method were performed in [Lam, 2005]:

Real-valued frequency independent reflection coefficient. This was computed by determining the admittance values out of the decay curve of the first few clearly separated room modes (see reference [Kuttruff, 1991] for more insight in this matter). This assumes that the admittance is real which is acceptable as long as the walls are acoustically hard, i.e. their impedance is high. Hence the reflection coefficient is also real. Admittance values for the materials involved were assumed to be constant within the frequency range of interest which was up to 100 Hz.

Complex frequency independent reflection coefficient. The previous assumption is based on the requirement that the existing walls are acoustically hard, providing very low random absorption coefficients typical of reverberation rooms for instance. In other enclosed spaces with more absorptive walls, a complex value for the admittance may be needed to keep suitable precision. In [Lam, 2005] a value of $(0.2, 0.2j)$ was arbitrarily assumed in this respect.

Complex frequency dependent reflection coefficient. Frequency dependent behaviour is characteristic of most, and especially absorptive materials. In order to perform a more realistic simulation, frequency dependent admittance values were introduced, calculated from an empirical model published by Delany and Bazley [1970].

5.2.2 Spherical Wave Reflection Coefficient

As it will be mentioned in section 5.3, the plane wave approximation is appropriate at high frequencies, for incidences close to normal, and for low absorptive surfaces. On the other hand for low frequencies, in the cases where the angle of incidence is far from normal and the surface presents high absorption, the spherical wave front may have a relevant effect. Only plane wave reflection coefficients will be considered in the present work. Therefore the spherical wave reflection coefficient is just briefly introduced.

The spherical wave reflection coefficient can be defined as given by equation 5.11 [Lam, 2005]

$$Q = R + (1 - R)F(w) \tag{5.11}$$

being R the plane wave reflection coefficient from either expression 5.4 or 5.10 and

$$F(w) = 1 + jw\sqrt{\pi}\exp^{-w^2} erfc(-jw) \tag{5.12}$$

the so-called boundary loss factor due to spherical wave front. In expression 5.12, $erfc$ is the complimentary error function and w denotes the numerical distance and is given by equation 5.13

$$w = \sqrt{jkR_2/2}(\beta + \cos\theta), \tag{5.13}$$

where the factor R_2 is the length of the reflected path.

It can be noted how the spherical wave reflection coefficient is a function of the plane wave reflection coefficient and also of the locations of both source and receiver. Furthermore, it involves the approximation of an infinite series (the $erfc$ term). As a result, this approach presents higher complexity and it is expected to require significantly larger computation time. On the other hand the accuracy provided is reported to be comparable to that of the BEM.

Lam [2005] implemented this method in several forms, as those previously presented for the admittance-based reflection coefficient.

5.2.3 Discussion

The real reflection coefficients are not able to fully represent the proper phase shift involved in a reflection and for that reason one may expect that using complex reflection coefficients will enhance the accuracy of the results.

In [Suh and Nelson, 1999] it was investigated the phase shift produced by a complex surface impedance. To achieve this task, the complex surface impedance was replaced by a purely positive real value providing the same absorption coefficient as the former. Predictions obtained by running a PISM for both cases were compared. That procedure revealed that the usage of complex surface impedance, and hence complex reflection coefficient, determines the accuracy of the model only when dealing with fairly absorptive surfaces. For less absorptive materials however, the effect of complex reflections turned out to be not that significant.

This conclusion was supported in subsequent work by Lam [2005], where real-valued admittances and hence reflection coefficients were reported to yield acceptable results for low absorptive walls. Further, Jeong et al. [2008] also coincide in the sense that expression 5.6 means no phase shift for those reflections taking place against low absorptive walls.

It should be noted that using complex values increases the computation load. An increase of 96 times for the PISM execution time with respect to the conventional ISM was reported [Suh and Nelson, 1999] for a medium sized (74 m^3) rectangular room with only the floor modelled by means of complex reflections.

It should also be noted that complex impedance values of surfaces are hardly ever at hand and measuring them can become a tedious task†. Appendix A gives a brief insight into the matter of obtaining the impedance of surfaces by several methods.

Regarding the angular dependence, the majority of the aforementioned methods present angular dependence with the incoming sound. The angle dependent real-valued reflection coefficient was found to produce more accurate predictions than those by the angle independent in a room with materials presenting different degrees of absorption [Jeong et al., 2008]. However the difference between the predictions was shown not to be very distinguished whereas the computation time was shown to increase significantly when considering the angular dependence.

It can be noticed as well how the complex reflection coefficient method is equivalent to the last version of the admittance-based methods.

It is expected that the PISM will yield more accurate results than the conventional ISM with any of the aforementioned methods. This holds even with that of equation 5.5, which involves no phase shift at reflection, since the phase shift due to the propagation path is included, thus accounting for the phase information partly.

†Among the previous works consulted for the present work, only that by Suh and Nelson [1999] performed complex impedance measurements, and for the minority of the materials involved.

Lastly, concerning the spherical wave reflection coefficient, it appears to provide a better performance than that of the plane wave reflection coefficient, mainly for highly absorptive surfaces where the latter is found to have noticeable errors. In fact, for simplified scenarios such as that considered in [Lam, 2005] where diffraction and scattering are neglected, it is reported to yield results that are very similar to those by the BEM in terms of accuracy.

To conclude, it seems that the real-valued reflection coefficients are more practical in the sense that they provide reasonable accuracy, depending on the characteristics of the materials, as well as ease in the computation. Therefore a trade off may be to characterize by the complex impedance only those surfaces whose materials are highly absorptive while approximating the rest.

5.3 Plane Wave Approximation

Let us suppose an scenario as that of figure 5.1 where the sound field at a receiver B is the contribution from both direct sound and a component reflected from the wall. For spherical wave incidence, the wall is hit at various angles and the reflected component is given by an expression function of the complex reflection coefficient of the wall and the Bessel function of zero order [Suh and Nelson, 1999].

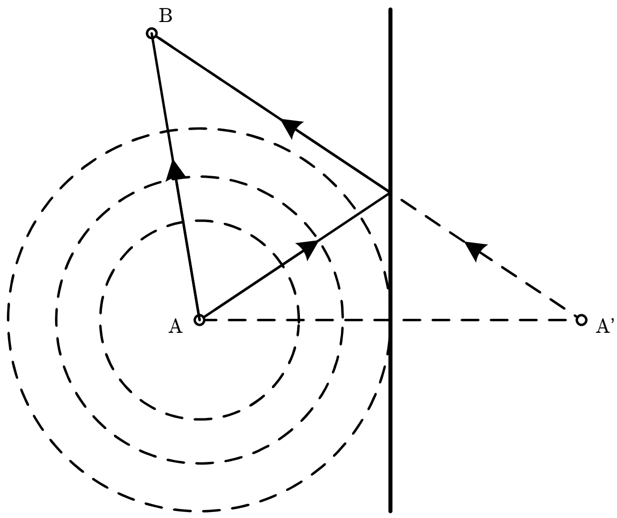

Figure 5.1: Spherical wave reflection with a wall.

An approximation of the reflected component can be performed by assuming a constant angle of incidence, i.e. a plane wave. The reflected component can be related to another image source A' located behind the wall that radiates spherical waves whose amplitude is reduced by the reflection coefficient. It must be noted that although a spherical wave is present, the reflection is computed for a constant angle of incidence. This means that *for the moment of reflection, the sound field model is switched to a plane wave* [Vorländer, 2008].

It must be noted that purely plane waves do not exist in real world. There are however certain conditions in which approximations of plane waves take place, such as sound waves travelling through a rigid tube. Furthermore, a limited region of a spherical wave can be regarded as a plane wave as long as the distance from the excitation point is large compared to all wavelengths involved [Kuttruff, 2000].

It has been shown in [Suh and Nelson, 1999] that the error due to the plane wave approximation is most sensitive to the angle of incidence. It is concluded that the approximation is sufficiently accurate except for grazing incidence† or highly absorptive surfaces when the source-receiver distance is less than a few wavelengths, i.e. low frequencies. The idea is that the larger the distances from the source to the wall and from the receiver to the wall, the lesser the error induced by substituting a spherical wave by a plane one.

In this respect Vorländer [2008] states that at grazing incidence and too close distances from of either source or receiver to the wall, systematic uncertainties in terms of sound pressure must be expected, which besides are audible. This implies that in the area located in the middle of a room, errors should be smaller than those present at positions close to the walls.

It can be noticed that for medium sized rooms (for instance up to 200 m^3) and at low frequencies (say below 200 Hz), it may be hard to find a centre area further than a wavelength from the walls. Hence in these scenarios the validity of this approximation is at its limits.

†Grazing incidence is given when the angle of incidence of the incoming sound is $\theta > 60$ ° [Vorländer, 2008].

Chapter 6

PISM Design and Implementation

This chapter concerns the design and implementation of the PISM. The design principle together with the different steps followed in the implementation are explained.

6.1 Design Principle

The design principle of the PISM is to add all complex pressures present in a pressure reflectogram at a given frequency, which are the contributions due all the considered image sources. Repeating this operation for a large number of frequencies, the complex steady-state transfer function between a source and a receiver is computed. The latter can be converted to an impulse response by inverse Fourier transformation. This approach was previously suggested in [Van Maercke, 1986][Suh and Nelson, 1999][Lam, 2005][Jeong et al., 2008] and it makes use of a predefined frequency resolution for the complex transfer function to be computed.

The design can be split into several tasks, which are subsequently described:

1. Determination of simulation initial setup.
2. Determination of image sources location.
3. Discard of invalid image sources.
4. Determination of the surface reflection factor R_{prod} associated with each image source.
5. Application of attenuation due to spherical radiation.
6. Frequency interpolation of the surface reflection factors R_{prod}.
7. Computation of the complex transfer function.
8. Determination of the RIR.

6.2 Determination of Simulation Initial Setup

Firstly, room dimensions L_x, L_y, L_z, original source coordinates S_x, S_y, S_z and receiver coordinates R_x, R_y, R_z must be defined.

The following parameters must be set as well:

- impulse response length†,
- sampling frequency,
- frequency resolution Δf for the complex transfer function and
- materials absorption coefficients in octave bands.

Based on the impulse response length and the room dimensions, the program determines the maximum order i_0 of reflection needed to compute such an impulse response, in a similar fashion as the example included in section 4.3. The order resulting as the product of impulse response length by reflections on average per second is normally a fractional number. Therefore it is rounded to the next integer. The amount of image sources N_{ISr} up to such an order is computed subsequently according to expression 4.2, which is included here again for completeness in equation 6.1

$$N_{ISr} = \frac{2}{3}(2i_0^3 + 3i_0^2 + 4i_0). \tag{6.1}$$

It should be noted that the frequency resolution Δf is not determined by the impulse response length. The frequency resolution is a parameter set by the user. The impulse response length only determines the amount of image sources that are considered for the computation. A limitation in the definition of the aforementioned parameters is that the number of points of the inverse Fourier transformation to be performed (which depends on the sampling frequency and the defined frequency resolution) must be greater than the desired impulse response length in samples.

†For the current work, the impulse response length is determined by that of the measured impulse responses at the standard listening room. Should the program be applied for the simulation of an enclosure without knowing this factor, it could be approximated by estimating the reverberation time, for instance with Sabine's or Eyring's formulae.

6.3 Determination of Image Sources Location

Coordinates of all image sources are determined according to expression 6.2 [Hammad, 1988]

$$X_i = (2nL_x \pm S_x), \qquad Y_i = (2lL_y \pm S_y), \qquad Z_i = (2mL_z \pm S_z) \tag{6.2}$$

where n, l and m are integers that theoretically range from $-\infty$ to ∞. In the current implementation they range within an interval whose limits are related to the maximum order of reflection i_0. This interval is restricted as much as possible while ensuring that all image sources required to fill up the impulse response are calculated.

6.4 Discard of Invalid Image Sources

Equation 6.1 leads to a number of image sources corresponding to a rounded maximum order of reflection. Because it is rounded, the number of image sources whose coordinates were found is larger than the actual number of image sources required. Therefore, once all the possible image sources are determined geometrically, those which actually contribute to the impulse response must be kept while the rest must be removed. According to Borish [1984], image sources providing information to the impulse response must fulfil three requirements.

Validity. Considering the boundaries of the room as mirrors with the reflective side facing the interior, a valid image source has to be reflected upon the reflective side of the boundaries. The other side is non reflective and consequently it should not be used to obtain any image source. The manner to meet this requirement is simply by not reflecting an image source across the wall used to create it.

Proximity. A desired impulse response length must be input to the program. Every image source is located at a certain distance from the receiver, corresponding to a delay with which the sound ray emitted arrives to the latter. Only those image sources whose rays arrive within the predefined impulse response length must be considered. This is how the ISM limits its computation, i.e. by rejecting image sources which are found to be too far from the receiver, with respect to a predefined threshold given by the impulse response length. There are other approaches of limiting the ISM computation, e.g. a maximum order to be considered. According to Borish, however, proximity is the most accurate.

Visibility. As discussed in section 4.3, if the room under consideration is rectangular all image sources are visible. The standard listening room used as case study is not completely rectangular, as will be seen in section 7.2.2. However it was regarded as rectangular, assuming certain amount of error.

6.5 Determination of the Surface Reflection Factor R_{prod}

The sound ray emitted by a certain image source strikes a number of surfaces prior to its detection by the receiver. The product of the reflection factors of the surfaces involved for every particular sound ray, i.e. associated with every particular image source, is determined. It is denoted as R_{prod} according to equation 6.3 [Allen and Berkley, 1979]

$$R_{prod} = \sum_{n=-\infty}^{\infty} \sum_{l=-\infty}^{\infty} \sum_{m=-\infty}^{\infty} \sum_{\bar{p}=0}^{1} R_{x1}^{|n-q|} R_{x2}^{|n|} R_{y1}^{|l-j|} R_{y2}^{|l|} R_{z1}^{|m-k|} R_{z2}^{|m|}. \tag{6.3}$$

In equation 6.3 the reflection factors for each of the six surfaces are denoted as R_{xi}, R_{yi} and R_{zi}, with i = 1,2, where the subindex 1 refers to the surface closest to the origin and subindex 2 to the opposing surface. The values n, l and m are the integers already used in equation 6.2. The sum over the vector $\bar{p}$ is actually used to indicate three sums, i.e. one for each of the three components of $\bar{p} = (q, j, k)$. It represents 8 different sets of values given by the 8 possible permutations.

The surface reflection factors can be defined in several ways in terms of frequency and angular dependence as well as nature of their values (real or complex). In the current implementation, the surface reflection factors are frequency dependent and at this point of the implementation they are defined in octave bands from 125 Hz to 1 kHz.

It is also at this point of the implementation where the different methods of modelling surface reflection factors described in section 5.2 can be introduced to account for the phase information.

6.6 Application of Attenuation due to Spherical Radiation

The distance r from every image source to the receiver is calculated. Subsequently the attenuation due to spherical radiation is applied for every particular image source multiplying R_{prod} of equation 6.3 by the term $1/r$ since we are dealing here with pressure amplitudes.

6.7 Frequency Interpolation of the Surface Reflection Factors R_{prod}

The surface reflection factors R_{prod} (including the attenuation by distance) associated to every image source are so far defined in octave bands. An interpolation in the frequency domain is to be performed from octave band values to the frequency resolution specified in the initial settings. The cubic spline interpolation was selected since according to Vorländer [2008] it is a well-qualified method for interpolating reflection factors.

6.8 Computation of the Complex Transfer Function

At this point of the implementation, the effect due to surfaces reflection and attenuation due to spherical radiation are determined. The next step is the core of the implementation, consisting of the computation of the complex steady-state transfer function† between the predefined source and receiver.

The procedure is explained with help of figure 6.1. Firstly, the pressure reflectogram between the source and receiver is computed for a given frequency. Figure 6.1a shows the magnitude of the pressure reflectogram at a given frequency.

The steady-state pressure p_{s-s} at such a frequency is shown in figure 6.1b and can be obtained by the summation of all the transient pressure components present in the pressure reflectogram of figure 6.1a. In figure 6.1b, the blue colour at the bottom part of the pressure magnitude bar represents the contribution to the steady-state pressure from the direct sound, arriving at a time t_1 in the reflectogram of figure 6.1a. In the same way, magenta and violet colours represent the contributions from the reflected transient pressure components arriving at time t_2 and t_3 respectively.

It must be noted that the transient pressure components are the contributions due to the original source and all the considered image sources. Every component is a complex pressure value according to the first term of equation 5.1 if it is due to the original source or according to equation 5.3 if it is due to an image source. Consequently the steady-state pressure is also complex valued.

By calculating steady-state pressures for all frequencies within the range of interest, the transfer function is constructed, which is shown in figure 6.1c. The frequency resolution Δf is that specified in the initial settings.

†For the remaining of this chapter it will be referred to as transfer function.

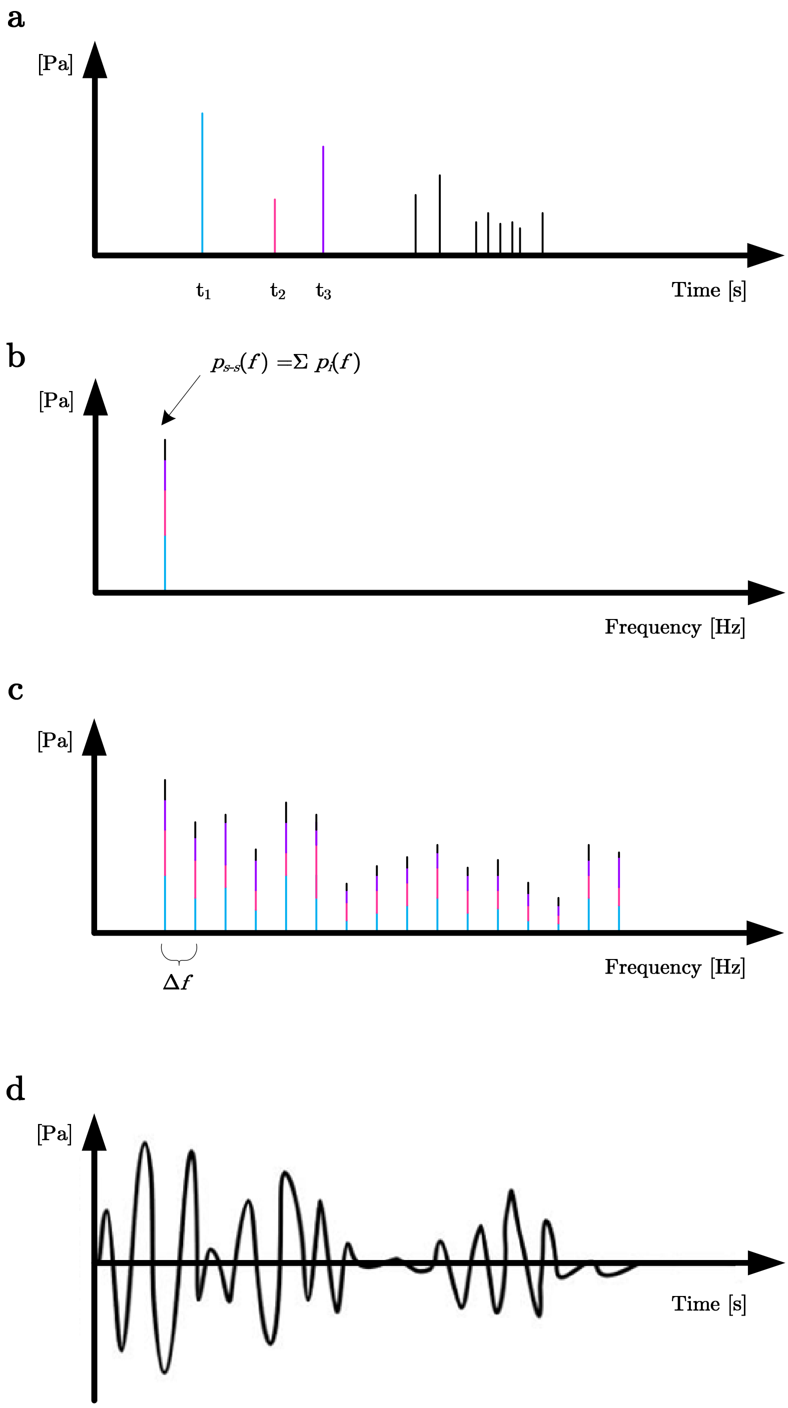

Figure 6.1: Computation procedure of the PISM in schematic drawings. (a) Pressure reflectogram. (b) Steady-state pressure within the steady-state transfer function, corresponding to the summation of the transient components of the pressure reflectogram of (a). (c) Steady-state transfer function. (d) Impulse response.

6.9 Determination of the RIR

The RIR, shown in figure 6.1d, can be computed from the transfer function by taking the inverse Fourier transform.

6.10 Considerations

6.10.1 Filtering

It was found out by Allen and Berkley [1979] an *apparently non physical behaviour of the model at zero frequency.* First simulated RIRs in the present work showed this effect, characterized by a cumulative offset leading to impulse responses superimposed over a positive slope.

This effect must be removed in some way. Allen and Berkley [1979] applied a low-frequency highpass filter to the computed RIR at a cutoff frequency of 0.01 times the sampling frequency. If the RIR is to be plotted in octave bands, this type of filtering is also suitable to remove this undesired effect. It should be noted that the filtering is applied to the simulated RIR, which in turn is derived from the previously computed transfer function. Therefore the influence of the filtering is not to be seen in the transfer function plot.

6.10.2 Attenuation due to Air Absorption

The attenuation due to air absorption should also be accounted for. Expression 4.4 is valid solely for frequencies within the range 1.5 to 10 kHz, which is above the considered frequency range in the simulation. Therefore air attenuation is not included in the model. However minor inaccuracies are expected regarding this issue due to the small dimensions of the room considered as a case study.

Chapter 7

Case Study: Standard Listening Room

This chapter presents the comparison between the measured data at the standard listening room and the results obtained by the simulation of the latter by means of the PISM. Firstly, a description of the room where the measurements were carried out together with relevant considerations regarding such a scenario are included. Then the preprocessing applied to the measured data prior to the comparison is explained. The settings defining the simulation are specified. Several manners to characterize reflections from the surfaces within the PISM are tested. The procedure for the evaluation of the implemented model is established. The results are shown and eventually discussed.

7.1 Purpose

The purpose of this chapter is to perform a comparison between

- measurements carried out at the standard listening room and
- results obtained by the simulation of the sound field in such a room by means of the PISM.

The comparison is intended to serve as an evaluation of the implemented model, in such a way that the measurements are considered the reference. The comparison is performed in both frequency and time domains.

7.2 Scenario

7.2.1 Room Selection

Several rooms were considered as possible scenario for the aforementioned purpose. The following criteria were taken into account.

Rectangular Geometry

It was previously explained in section 4.3 that applying the ISM (and hence the PISM) to a non rectangular geometry means that not all the image sources are visible. Therefore a visibility check must be carried out to find those image sources which actually contribute to the response, increasing thus the complexity of the implementation. It is not considered the goal of this work to develop the case for an irregular geometry since the effect of the phase information can be studied in the scenario of a rectangular room.

In addition, a scenario presenting as little diffusion and diffraction as possible is desired, since the ISM does not account for those phenomena.

Volume

The room should be large enough to allow appropriate distances from source to receiver and from them to the reflecting surfaces in order to perform measurements following guidelines in the ISO 3382 standard [ISO 3382, 1997].

On the other hand it is desired a relatively small room in such a way that a modal distribution is present. Thus the PISM can be challenged to account for that wave related phenomenon.

Rooms previously used in other works [Suh and Nelson, 1999][Lam, 2005][Jeong et al., 2008] meeting the requirements above present a volume of between 70 and 90 m^3.

Materials

The ideal situation is that in which every wall in the room presents uniform characteristics, i.e. no material discontinuities in the wall. In this way diffusion and diffraction are minimized.

Furthermore, it would be interesting to have a room with both absorptive materials and acoustically hard materials. As previously discussed in section 5.2 they can be characterized following different approaches. Hence it could be interesting to see the influence of modelling them in distinct ways.

Room Selection: Standard Listening Room

According to the criteria stipulated above, the standard listening room is the most adequate room of all available at the facilities of the Section of Acoustics, Aalborg University.

7.2.2 Room Description

The standard listening room is described next, according to the aforementioned criteria. The room can be seen in several pictures in figure 7.1 showing the details to be commented in the following. The room description can also be found in appendix B which contains the measurement report of the measurements carried out.

(a) Window and plastic ducts. **(b)** Oblique surface and ceiling structure.

(c) Plaster surface for flush mounted speakers. **(d)** Different carpets.

Figure 7.1: Details of the standard listening room where the measurements were carried out.

Geometry

The standard listening room is a quasi rectangular enclosure. The only deviation from the rectangular geometry is due to the ceiling, which is made of suspended boards. The boards are located horizontally except for the series of boards adjacent to three out of the four walls, which are located obliquely. For the measurements those parts were arranged so that all the boards were located horizontally. However above the former oblique boards there is an oblique surface of around 2 m^2 hiding a pipe from the ventilation system, which is located at the top of one of the walls and occupies half of its length. This surface was the only item causing the non rectangular shape of the room.

It must be noted that the structure for the holding of the former oblique boards was still present when the measurements were carried out. There are also several connection panels and plastic ducts with rectangular section housing wires inside. Since the dimensions of these elements are small, the frequencies in which they could produce error in the simulations are relatively high.

Volume

The dimensions of the standard listening room are 7.8 m long, by 4.14 m wide, by 2.76 m high yielding a volume of 89 m^3.

Materials

The walls are concrete made, except a little window of around 0.34 m^2 at wall $y = 0$ (see figure B.1) and an area made of plaster of around 2.15 m^2 in the centre of wall $y = 7.8$. Furthermore, there is a double door with metallic coverage from the inside located at wall $x = 4.14$.

The floor is wooden made, except for a little area of glazed tile at the end of the dimension y with a surface of around 3 m^2, occupying the whole room width. For the measurements however the floor was covered with carpet. Most of the floor surface was covered with one carpet, but there was an area of around 6.2 m^2 that had to be covered with other types of carpet.

The ceiling is made of 16 mm thick chip wood boards located at a height of 2.76 m above the floor, which are suspended from a concrete ceiling at 3.05 m above the floor. The oblique surface covering the pipe from the ventilation system is also made of chip wood.

Schroeder Frequency

The Schroeder frequency of a room is given by the equation 7.1 [Kuttruff, 2000]

$$f_c = k\sqrt{\frac{RT}{V}} \tag{7.1}$$

where k is a constant of value 2000, RT is the reverberation time and V is the volume of the room. This is the frequency at which the overlap between room modes start to be significant.

The standard listening room presents a volume of 89 m^3 and a measured reverberation time of 1.07 s, yielding a Schroeder frequency of $f_c = 219$ Hz.

7.2.3 Uncertainties due to Room Condition

The implemented model simulates a rectangular room whose surfaces present uniform materials. The conditions of the standard listening room are therefore not ideal. There are several aspects that are either wrongly modelled in the simulation or simply not accounted for. Furthermore the ISM neglects both diffusion and diffraction as already mentioned.

Non rectangular room geometry. Because of this there is a number of missing image sources that should be considered in the model. Likewise, there is a number of computed image sources that are actually wrong.

Connection panels and plastic ducts. They produce some mistakes related to the considered image sources in a similar fashion as the previous point, although in a lesser extent. In addition, they cause mainly sound diffusion at high frequencies.

Lamps and ceiling oblique structure. They lead to a certain amount of diffusion and diffraction.

Materials discontinuity. There is no fully uniform surface in regard to its material. In the floor several types of carpet were displaced to cover the entire surface (see pictures in figure 7.1). Likewise, neither the door nor the window or the plaster surface were modelled in the simulation. This fact involves a mismatch in the absorptive properties of the modelled surfaces as well as certain amount of diffraction due to the existence of boundaries between materials with different impedance.

Because of the aforementioned issues, certain degree of uncertainty is expected in the simulation results. It is desired as well as complex to determine the order of magnitude of such an uncertainty with the aim of performing a more representative evaluation of the model. However it was not possible to accomplish this task thoroughly due to time limitations.

7.3 Measurements Preprocessing

RIRs were acquired at the standard listening room at a sampling frequency of 51.2 kHz. From their acquisition to the actual comparison of the measured data with that simulated, the following preprocessing was carried out:

1. Source deconvolution.

2. Signal resampling.
3. Filtering.

These tasks are briefly described next.

7.3.1 Source Deconvolution

The purpose of the measured RIRs is to provide a reference with which to compare those obtained by simulation.

The RIRs computed in the simulations carry information only of the room, i.e. its geometry and materials. Both sound source and microphone were regarded as ideal, being omnidirectional and providing flat frequency response.

On the contrary, RIRs measured at the standard listening room contain information not only from the room but also from the equipment chain used to perform the measurements. The amplifier and measurement microphone provide practically flat transfer function and hence their effect can be considered negligible. However the transfer function of the omnidirectional source used for the measurements is not flat and therefore its effect must be removed if a fair comparison is to be conducted[†]. The goal is to invert the transfer function of the omnidirectional source and apply it to the measurements, so as to get rid of the source effect. This task can be done by means of inverse filtering.

The measured transfer function of the omnidirectional source was taken from previous work by the author [08gr961, 2008]. Such a transfer function was inverted by means of the LPC technique. The LPC algorithm yields a set coefficients that model the transfer function under consideration as an all-pole system. Filtering the measured RIRs with an FIR (all-zero system) filter built up from the aforementioned set of coefficients leads to RIRs free of source effect. The LPC order was set to the value of 3000 and the deconvolution achieved can be seen in figure 7.2.

The deconvolution is satisfactory at mid and high frequencies. Nevertheless the inverse filter cannot properly compensate for the irregularities of the transfer function at the lower end of the frequency range, as figure 7.2 shows. It can be stated that the measured data are free from source effect from 60 Hz on. On the contrary deviations of ± 5 dB below 30 Hz and ± 2 dB from 30 Hz to 60 Hz due to the source response are found.

As a result of the deconvolution process, figure 7.3 shows the frequency response measured at position R2 in the standard listening room (see appendix B) and the frequency response after the sound source deconvolution.

[†]The omnidirectional source B&K 4296 behaves omnidirectionally up to around 4 or 5 kHz [B&K, 1989] which includes well the frequency range considered in the simulations. Otherwise its directional effect would have to be compensated for.

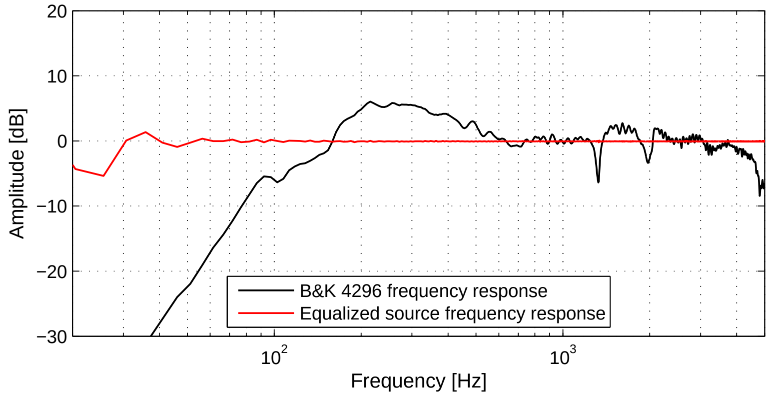

Figure 7.2: B&K 4296 source equalization. Black line depicts the source frequency response. Red line depicts the equalized response.

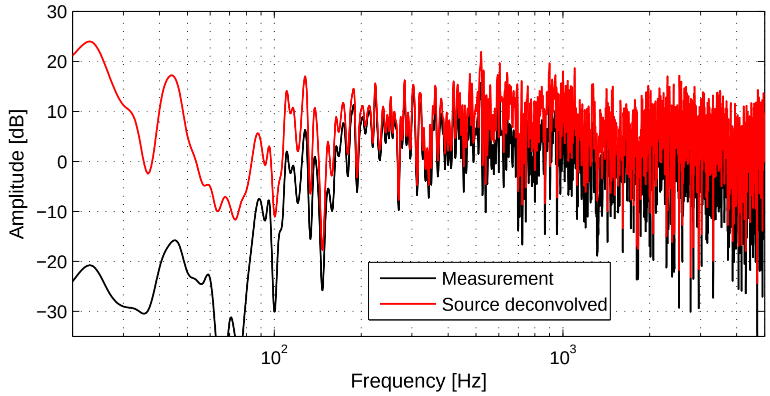

Figure 7.3: Frequency response measured at position R2 in the standard listening room, prior (black) and after (red) the sound source deconvolution.

7.3.2 Resampling

After deconvolving the sound source, the resulting RIRs were resampled to a sampling frequency of 12.8 kHz, which is the sampling frequency used for the simulations.

7.3.3 Filtering

RIRs were eventually filtered in the octave bands of 125, 250, 500 and 1k Hz for subsequent comparison with the simulation results.

7.4 PISM Simulation

7.4.1 Simulation Initial Setup

The simulations were carried out according to the following parameters.

Impulse Response Length

The modified standard listening room where the measurements were carried out turned out to be a quite reverberant scenario. The measured reverberation time was of around 1 s. To compute the entire impulse response was considered impractical since, as demonstrated in section 4.3, the ISM computation time increases exponentially with the impulse response length. It was proved how to compute the entire impulse response took several hours, causing as well problems related to memory handling, since the implemented software was not optimized in this respect. For all these reasons a trade off value of 200 ms was considered appropriate for the evaluation of the impulse responses.

Sampling Frequency

The selected value was 12.8 kHz being a compromise between computation time and accuracy. It allows to obtain smooth curves for the representation of the impulse responses.

Frequency Resolution

As explained in section 6.8, the transfer function is created by adding complex pressures for every frequency bin. Hence it is necessary to set a frequency resolution for the model. A value of 1 Hz was considered suitable based on previous work [Lam, 2005]. Higher resolutions can however be used [Jeong et al., 2008][Jeong and Ih, 2009] yielding more accurate predictions at the expense of increasing the computation load.

Simulation Frequency Range

The frequency range considered for the simulation is limited by the following factors:

- **Omnidirectional source frequency range.** The source considered in the model is omnidirectional, i.e. it provides the same frequency response regardless the direction of radiation. The source utilized for the measurements fulfil such a requirement up to around 4 or 5 kHz [B&K, 1989].

- **Materials characterization data.** Usually absorption charts from materials are given in either octave or one-third octave bands up to 4 or 8 kHz. However information from the ceiling material was found only up to the 500 Hz octave band.

In light of the limitations above, it was decided to set the frequency range for the simulation up to the 1 kHz octave band. Information from the ceiling material for such a band was extrapolated from the 500 Hz octave band to its same value.

The audible spectrum can be divided into four regions [De Geest and Patzold, 1996].

- **Region A**. The very low frequency region, delimited by $f < c/2L$ being L the largest room dimension. This is the frequency of the lowest axial room mode, i.e. below it there is no resonant support from the room. For the standard listening room region A is restricted below 22 Hz.
- **Region B**. Starting where region A ends and extending up to the Schroeder frequency f_c. In this region room dimensions are comparable to the wavelength of sound. There are prominent maxima in the frequency response due to the modal effect.
- **Region C**. The lower boundary is the Schroeder frequency f_c and the upper boundary is four times f_c. In this region a large number of room modes are excited and clustered together.
- **Region D**. Starting where region C ends. This is the higher part of the spectrum where the wavelengths are small if compared to room dimensions and thus geometrical acoustics prevail. For the standard listening room, region D is restricted above 876 Hz.

The frequency range considered for the simulation contains regions A, B and C entirely. In addition, region D is partly reflected.

Materials Characterization

The materials present at the standard listening room were specified in section 7.2.2. The absorptive properties of those materials could not be measured due to time limitations, being the most precise approach. Instead, such properties were taken from tabulated data found in the literature as shown in table 7.1.

7.4.2 Modelling of the Reflection Coefficients

Several methods of modelling the reflection coefficients of surfaces were described in section 5.2. Due to time limitations, the only method implemented was the angle independent real-valued reflection coefficient.

			Absorption coefficient α_{ran}				
Surface	Material	Description	125	250	500	1000	Reference
Floor	Carpet	5 mm thick, on hard floor	0.02	0.03	0.05	0.10	[CATT, 2002]
Walls	Concrete		0.02	0.02	0.02	0.02	[Vorländer, 2008]
Ceiling	Chip wood	16 mm thick, 9.9 kg/m^2, 30 mm away from real wall	0.27	0.07	0.01	-	[PTB, 2009]

Table 7.1: Definition of materials in the implemented model.

7.4.3 Uncertainties due to Simulation Model

Materials Characterization

The absorptive properties of the materials had to be guessed. Following a visual inspection of the materials, data were searched in the literature. Whereas concrete is quite well defined in charts, there are many types of carpets with different features apart from thickness. On the other hand, the data from the chip wood was sparse and incomplete, although it is expected that this material provides practically no absorption in high frequencies. These factors result in uncertainty in the simulation results. The most secure choice is measuring the materials.

Source Output Power

According to Kuttruff [2000], if the sound pressure in a room is to represent properties thereof and not from the sound source two requirements must be met:

1. An omnidirectional sound source is to be used.
2. Its output power is to be accounted for by an adequate normalisation.

The first requirement is met in the present work. Concerning the second one, if the source output power is known one can either apply an adequate normalisation to the measurements or introduce such an information in the model so as to have both measurements and simulation results with matching amplitude.

However the source output power was not measured. Therefore it was decided to normalize both measured and simulated impulse responses regarding their respective maximum amplitude value. In this way absolute information of the amplitude is lost whereas a comparison in terms of relative shape can still be done.

7.5 Evaluation

Based on the configuration established so far, the implemented model consisting of the PISM algorithm with angle independent real-valued reflection coefficients is tested.

7.5.1 Evaluation Design

The angle independent real-valued reflection coefficient given by equation 5.6 can be expressed in either positive or negative form. As mentioned in section 5.2 the positive sign is to be applied for reflections taking place with acoustically hard materials [Rindel, 1993][Suh and Nelson, 1999][Jeong et al., 2008]. Contrarily, reflections with soft materials are associated with the negative sign [Rindel, 1993][Jeong et al., 2008]. As a rule of thumb, heavy and dense materials, e.g. concrete and/or wooden panels should be regarded as hard whereas porous absorbers should be assumed to be soft [Rindel, 1993].

Based on previous considerations four conditions were defined as follows.

- **Condition 1.** All materials are considered acoustically hard. Hence the reflection coefficients are positive for all surfaces.
- **Condition 2.** All materials are considered acoustically hard except that of the floor. Hence the reflection coefficients are positive for walls and ceiling and negative for the floor.
- **Condition 3.** Wall material is considered acoustically hard whereas floor and ceiling materials are considered acoustically soft. Hence the reflection coefficients are positive for walls and negative for the floor and ceiling.
- **Condition 4.** All materials are considered acoustically soft. Hence the reflection coefficients are negative for all surfaces.

Due to the not so high absorption provided by any of the materials in the room, condition 1 is expected to be the closest representation of the actual room. The latter condition was inspired by previous work by Lehmann and Johansson [2008].

7.5.2 Evaluation Procedure

The evaluation of the implemented model throughout the four conditions is performed as a comparison of measurements and simulation results in both frequency and time domains. The evaluation is based on a determined measurement point in the standard listening room, whose coordinates can be found in appendix B.

Frequency Domain Comparisons

Frequency responses are compared by visual inspection. They are only plotted up to 500 Hz to ease their comparison since above that frequency the large amount of peaks and dips makes it difficult to perform an evaluation. It should also be noted that the frequency responses calculated from the measured impulse responses are computed based on the initial 200 ms of the latter. This is done in order to accomplish a fair comparison since the simulated frequency responses are obtained considering such a duration of the impulse response†.

A normalization in amplitude was performed in order to show both measured and simulated frequency responses around 0 dB. It should be noted that this is merely and arrangement for the presentation of the plots. The absolute amplitude information is not provided. For that reason the reader should focus on the shape of the frequency responses and not on the absolute amplitude.

Time Domain Comparisons

Pressure impulse responses and energy impulse responses in the octave bands of 125, 250, 500 and 1k Hz are compared by visual inspection.

The measured impulse responses begin their curves towards negative amplitudes due to the effect of the condenser microphone used for the measurements. This effect is not present in the simulated impulse responses, which have the opposite behaviour. Therefore the simulated pressure impulse responses shown in the following are inverted to account for this effect, in order to allow a proper comparison.

The energy impulse responses are obtained by squaring the pressure impulse responses and subsequently integrating them in time intervals with a specified time resolution. Each time interval has a duration of 1.01 ms and the initial 100 ms of the energy impulse responses are displayed.

In an attempt to achieve a more objective evaluation, the accuracy of the simulated energy impulse responses is assessed by the error measure E given by equation 7.2 [Suh and Nelson, 1999]

$$E = \left(\frac{\sum_{n=1}^{50} |e_{meas}(n) - e_{model}(n)|}{\sum_{n=1}^{50} e_{meas}(n)} \right) \cdot 100 \qquad [\%], \tag{7.2}$$

where $e_{meas}(n)$ and $e_{model}(n)$ are the measured and simulated energy impulse responses respectively, at the nth time interval. For the computation of the error measure E the initial 50 time intervals were considered, i.e. approximately the initial 51 ms of the energy impulse response.

† In terms of amount of considered image sources.

7.5.3 Evaluation Results

Frequency Domain Comparisons

Figure 7.4 shows the measured and simulated frequency responses at position R4 for the four conditions considered.

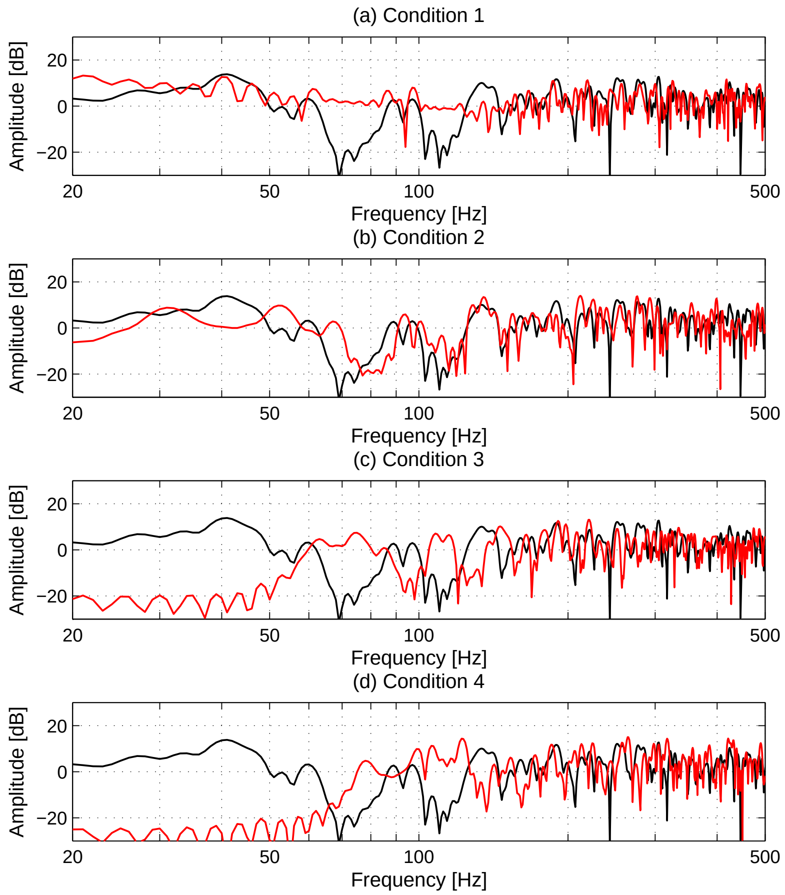

Figure 7.4: Comparison of measured and simulated frequency responses at position R4 for the four conditions considered. Black lines depict the measured frequency response (same in all plots). Red lines depict the simulated frequency responses.

It can be seen in figure 7.4 that for the frequencies below 60 Hz the simulated frequency responses in conditions 1 and 2 reflect to some extent the measurement. On the contrary simulated frequency responses in conditions 3 and 4 are far from being close to the measured one in that frequency range. Above 60 Hz, it can be noticed that simulated frequency responses in conditions 1 and 2 present an overall trend closer to the measurement than those in conditions 3 and 4.

This suggests that modelling the chip wood ceiling as a soft surface is not suitable. In addition, the approach followed by Lehmann and Johansson [2008] of defining negative reflection coefficients for all surfaces appears not to be satisfactory.

Apart from that, it can be seen in figures 7.4b, 7.4c, and 7.4d that the simulated frequency responses in the respective conditions seem to present a displacement in frequency with respect to the measurement. This can be seen for condition 4 around 100 Hz and more clearly for conditions 2 and 3 in the regions from 60 to 110 Hz and from 100 to 150 Hz respectively. The exact reason for this phenomenon is not known.

Figure 7.5 depicts a zoomed version of the measured and simulated frequency responses of figures 7.4a and 7.4b. They are displayed up to the Schroeder frequency for the standard listening room.

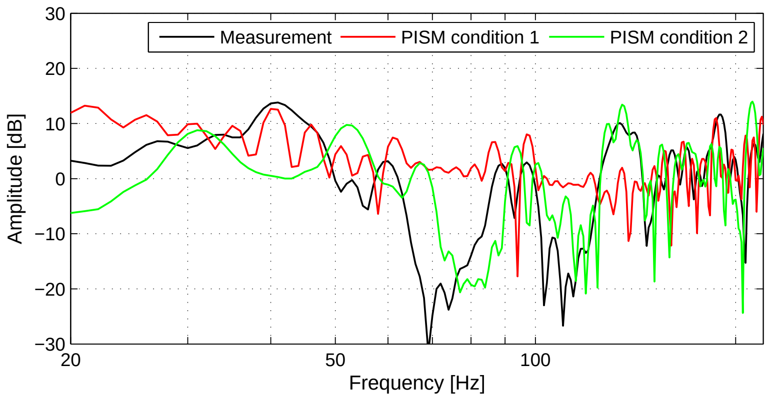

Figure 7.5: Comparison of measured and simulated frequency responses at position R4 for conditions 1 and 2. Black line depicts the measured frequency response. Red line depicts the simulated frequency response in condition 1. Green line depicts the simulated frequency response in condition 2.

By visual inspection of figure 7.5 it can be seen how up to around 60 Hz the frequency response simulated in condition 1 resembles the measurement to a larger extent than that of condition 2. From that frequency above, simulated frequency response in condition 1 reflects the region around 95 Hz quite well, especially the peak at 97 Hz, whereas it fails to represent most of the dips displayed in the measured frequency response. Simulated frequency response in condition 2 is able to reflect the peak around 140 Hz as well as the dip at 205 Hz and in general it provides more accurate representation of the dips than that of condition 1. However it shows the already mentioned displacement in frequency which can be appreciated from 60 to 110 Hz. In the latter frequency region, if the displacement were removed good agreement with the measurement would be found.

Time Domain Comparisons

Figures 7.6, 7.7, 7.8 and 7.9 show the measured and simulated pressure impulse responses at position R4 for the four conditions considered and in the octave bands of 125, 250, 500 and 1k Hz respectively. It should be noted that the displayed time lengths of the impulse responses were halved with increasing the frequency by an octave to ease their comparison.

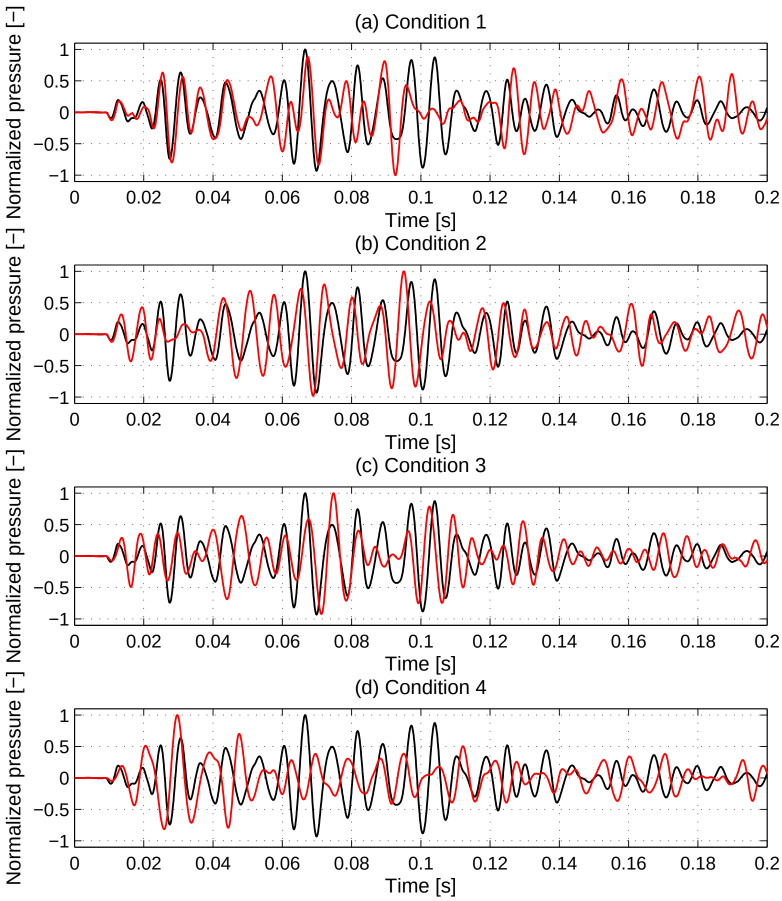

Figure 7.6: Comparison of measured and simulated pressure impulse responses at position R4 in the 125 Hz octave band for the four conditions considered. Black lines depict the measured pressure impulse response (same in all plots). Red lines depict the simulated pressure impulse responses.

In figure 7.6, differences between simulated and measured data can be found for the 125 Hz octave band. The impulse response simulated in condition 1 seems to be the most accurate, mainly in its early part, whereas the largest errors are shown in the impulse response simulated in condition 4. The results that can be inferred for conditions 2 and

3 are not very conclusive.

It can be noticed that the direct sound from source to receiver matches well between simulations and measured data. This observation holds as well for the rest of the octave bands considered (see figures 7.7, 7.8 and 7.9).

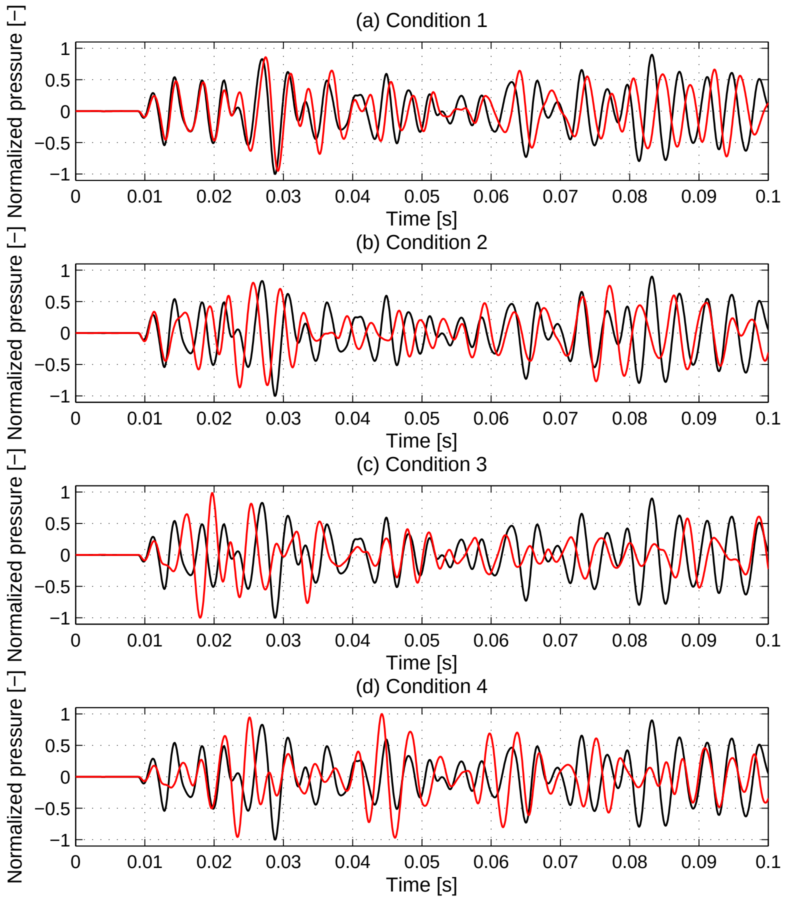

Figure 7.7: Comparison of measured and simulated pressure impulse responses at position R4 in the 250 Hz octave band for the four conditions considered. Black lines depict the measured pressure impulse response (same in all plots). Red lines depict the simulated pressure impulse responses.

Better results in terms of peaks definition and overall trend are found for the simulated impulse responses in conditions 1 and 2 in the 250 Hz octave band, as shown in figure 7.7. Simulated data in conditions 3 and 4 present larger differences than those in conditions 1 and 2, regarding the measured data.

For the 500 Hz octave band, the impulse response simulated in condition 1 shows good agreement with the measurement during the whole impulse response, as seen in figure

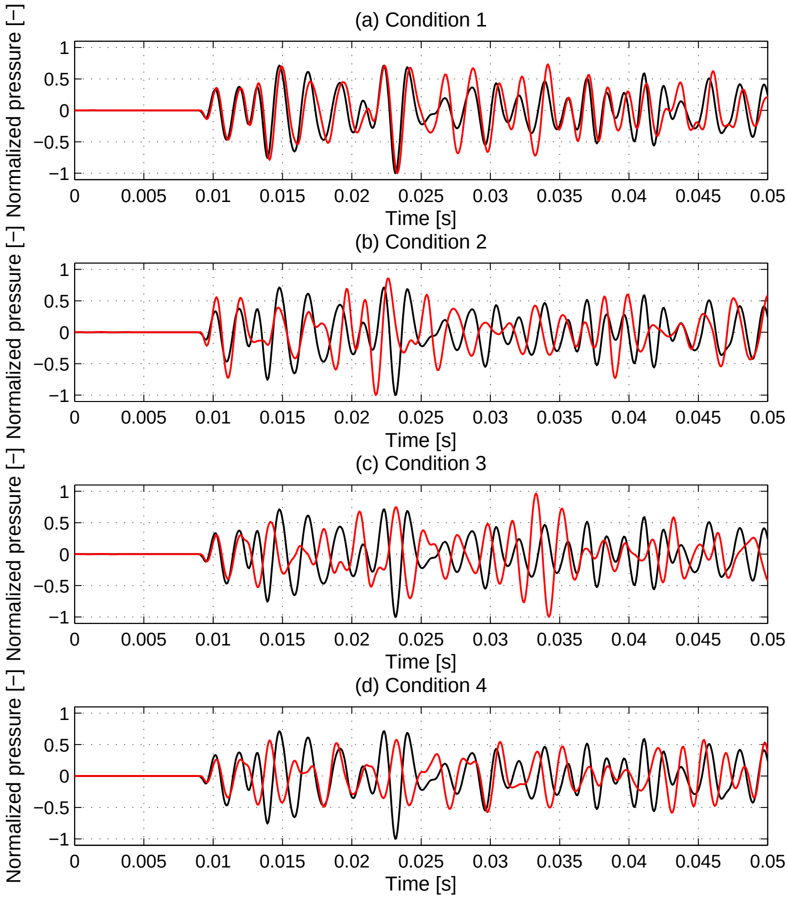

Figure 7.8: Comparison of measured and simulated pressure impulse responses at position R4 in the 500 Hz octave band for the four conditions considered. Black lines depict the measured pressure impulse response (same in all plots). Red lines depict the simulated pressure impulse responses.

7.8. Its early part is especially well predicted. Apart from that, similar results as those found for the 250 Hz octave band can be seen for the rest of the conditions.

In figure 7.9 for the 1 kHz octave band, it can be noticed the best performance of the simulation in condition 1, followed by that in condition 2. Less accurate results are found for conditions 3 and 4. The accuracy is higher in the early part of the impulse responses for all the conditions, mainly in condition 1.

In light of the results displayed so far in the time domain, simulations in condition 1 followed by those in condition 2 present the largest agreement with measured data, in terms of overall trend and peaks definition. Likewise, they provided best results in the frequency domain. Therefore they will be the only conditions considered in the following.

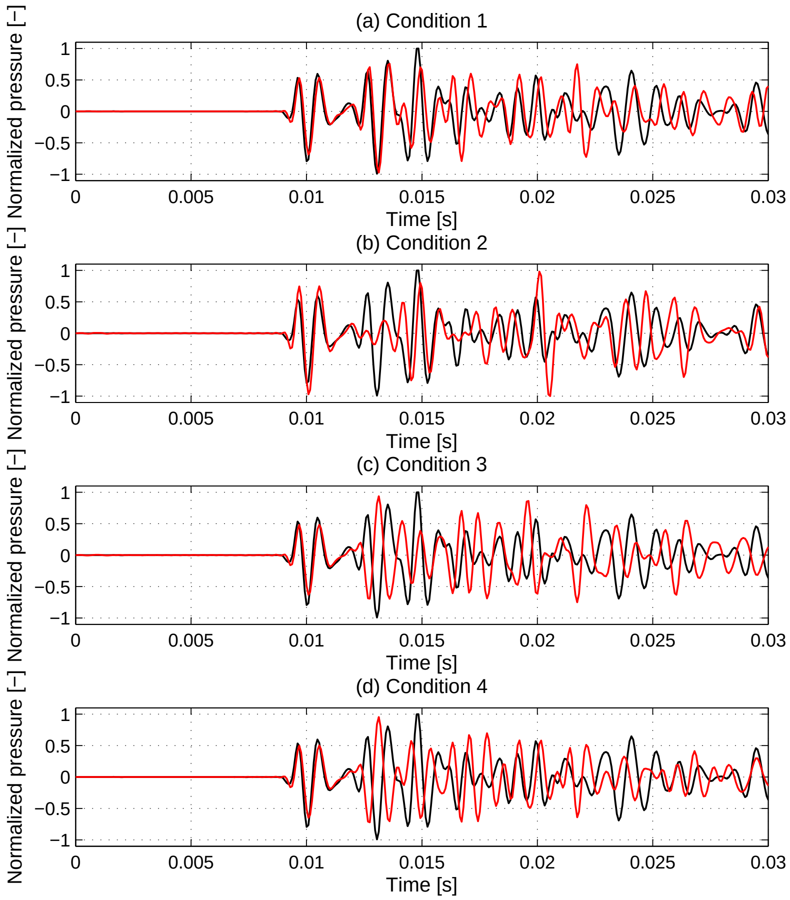

Figure 7.9: Comparison of measured and simulated pressure impulse responses at position R4 in the 1 kHz octave band for the four conditions considered. Black lines depict the measured pressure impulse response (same in all plots). Red lines depict the simulated pressure impulse responses.

The most accurate predictions seem to be found for the octave bands of 250 and 500 Hz, followed by those of 1 kHz. Furthermore, early parts of the impulse responses present higher accuracy than late parts.

So far, figures 7.6, 7.7, 7.8 and 7.9 show fractions of impulse responses whose time lengths displayed depend on the frequency, thus enabling a more precise comparison. Next, an evaluation based on a more overall impression is performed by showing the complete simulated pressure impulse responses at position R4. It should be noted that the signals plotted next are the same as before, but this time responses up to 200 ms are presented. They can be seen for the octave bands of 125, 250, 500 and 1k Hz in figures 7.10, 7.11, 7.12 and 7.13 respectively.

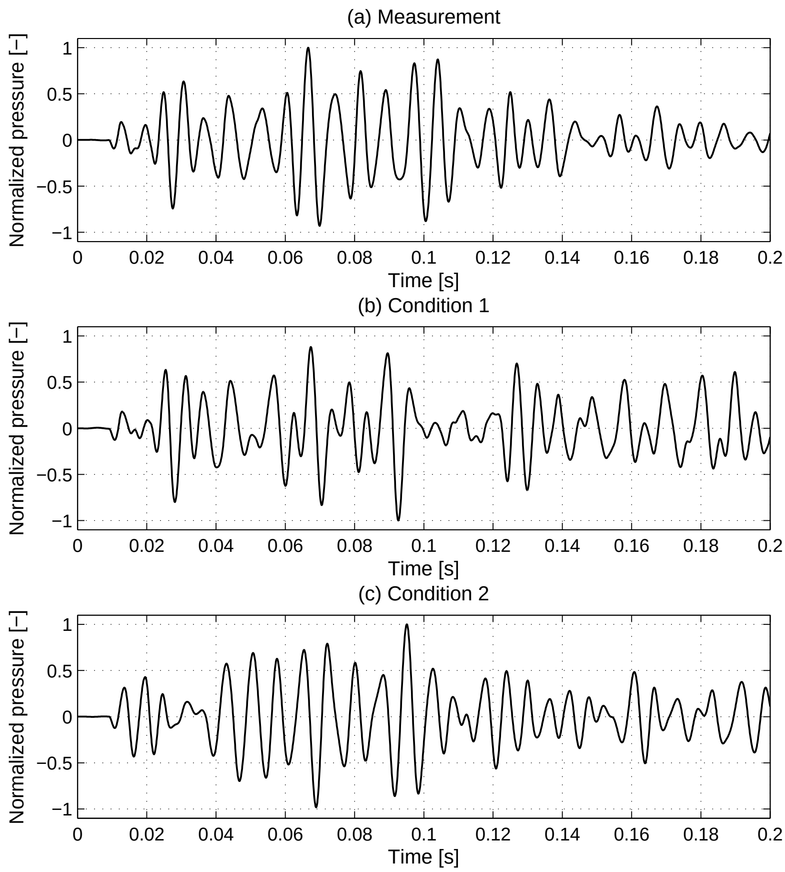

Figure 7.10: Comparison of measured and simulated pressure impulse responses at position R4 in the 125 Hz octave band for conditions 1 and 2.

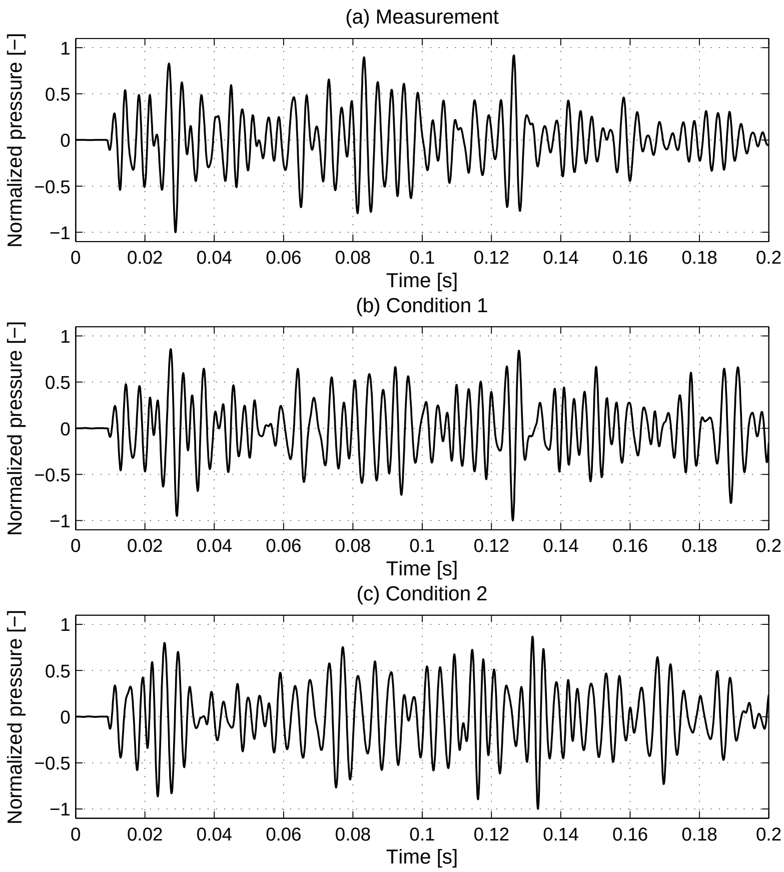

Figure 7.11: Comparison of measured and simulated pressure impulse responses at position R4 in the 250 Hz octave band for conditions 1 and 2.

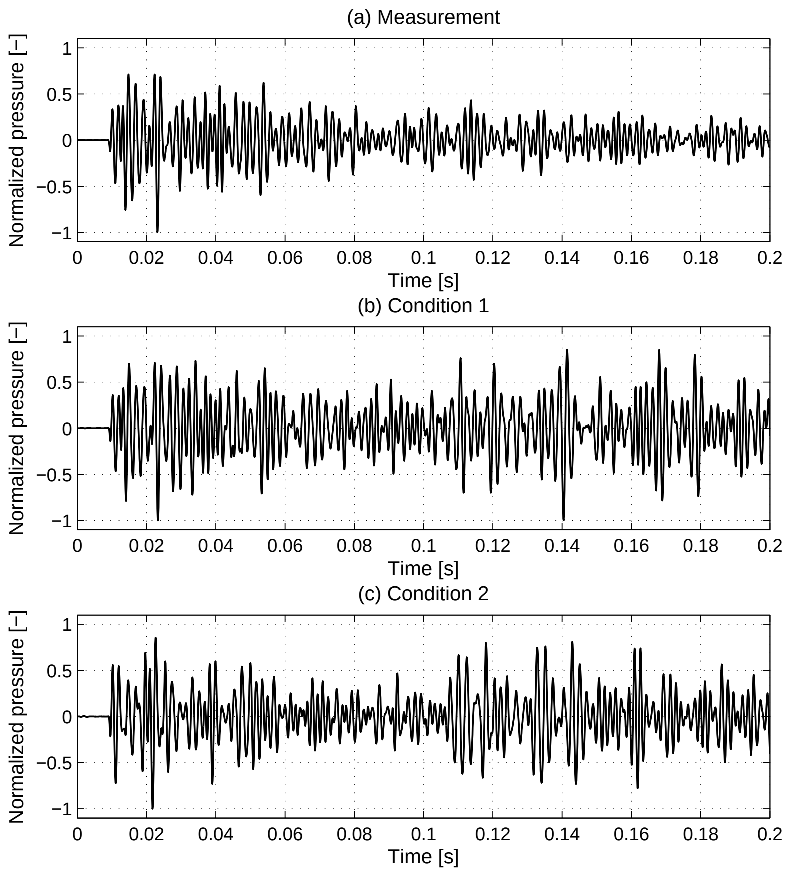

Figure 7.12: Comparison of measured and simulated pressure impulse responses at position R4 in the 500 Hz octave band for conditions 1 and 2.

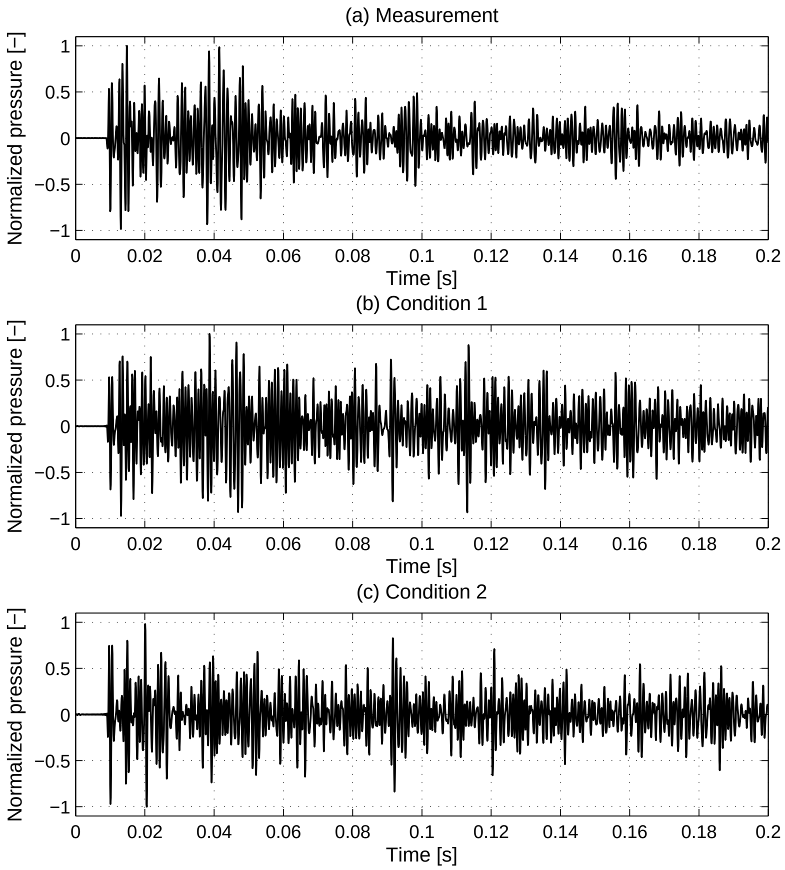

Figure 7.13: Comparison of measured and simulated pressure impulse responses at position R4 in the 1 kHz octave band for conditions 1 and 2.

Simulated impulse responses in condition 1 seem to present the most accurate results in all the considered octave bands as can be seen in figures 7.10, 7.11, 7.12 and 7.13. However the difference with respect to simulated data in condition 2 is not that large. As a general trend for all considered bands, early parts of impulse responses are better predicted whereas simulations fail to model properly the decay present in the measurements. This fact can be noticed especially in the simulated data in condition 1.

As an example, figure 7.8 showed an excellent agreement between the measured and simulated impulse response in the 500 Hz octave band for condition 1. It must be noted however that the impulse response length displayed is 50 ms. It can be seen in figure 7.12 for the same band and condition that effectively the early part of the impulse response resembles the measurement to a large extent. On the contrary, the late part of the impulse response show deviations from the measurement.

Another approach for displaying time domain results is by showing the energy impulse responses computed from the previous pressure impulse responses. It has the advantage that allows comparing results from both the PISM and the conventional ISM. The latter is based on energy addition and thus is unable to provide pressure impulse responses. Due to time limitations, results from the conventional ISM are not shown here. In light of previous work by Suh and Nelson [1999], energy impulse responses from the conventional ISM are expected to show a quasi monotonic decay, providing less accurate predictions than those by the PISM, which are included next.

Figures 7.14, 7.15, 7.16 and 7.17 show the measured and simulated energy impulse responses at position R4 for conditions 1 and 2 in the octave bands of 125, 250, 500 and 1k Hz respectively. The results displayed are supported by the accuracies of the simulated energy impulse responses, given by the error measure of equation 7.2. The error measures are listed in table 7.2.

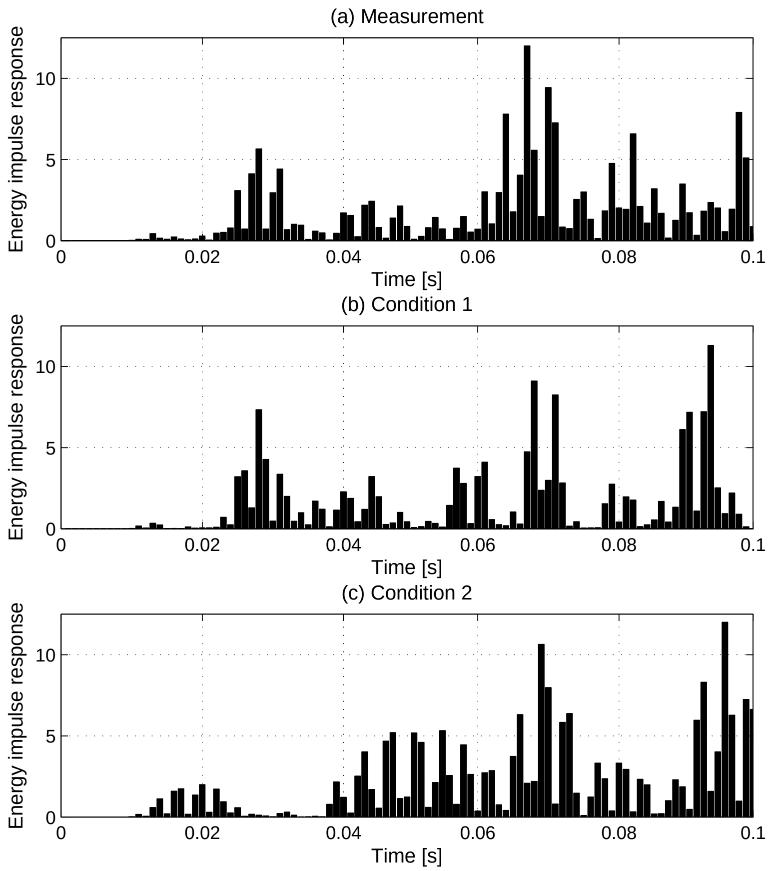

Figure 7.14: Comparison of measured and simulated energy impulse responses at position R4 in the 125 Hz octave band for conditions 1 and 2.

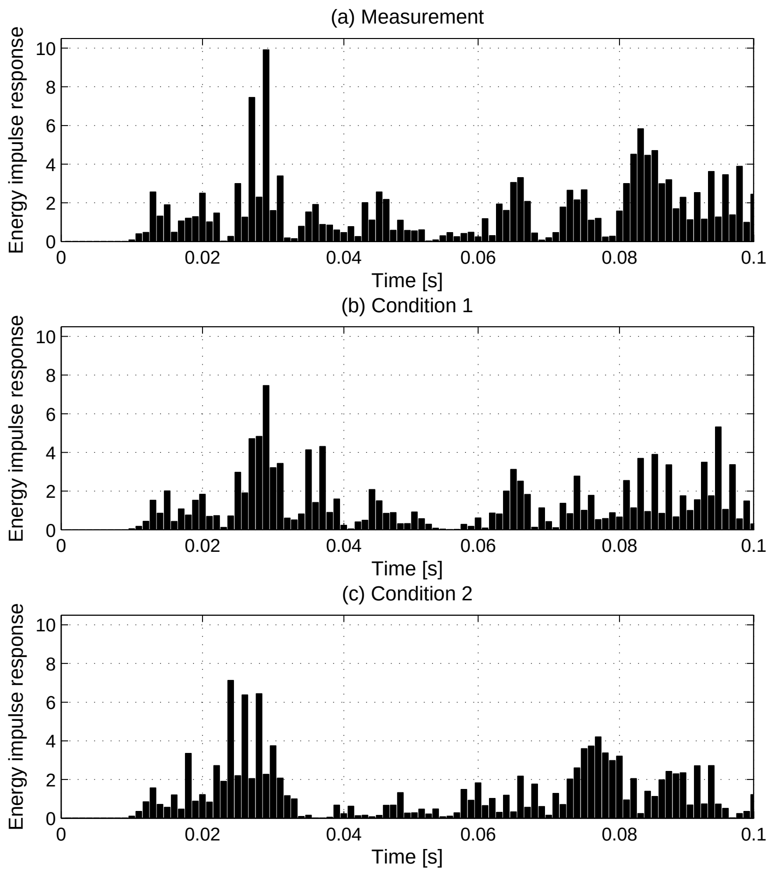

Figure 7.15: Comparison of measured and simulated energy impulse responses at position R4 in the 250 Hz octave band for conditions 1 and 2.

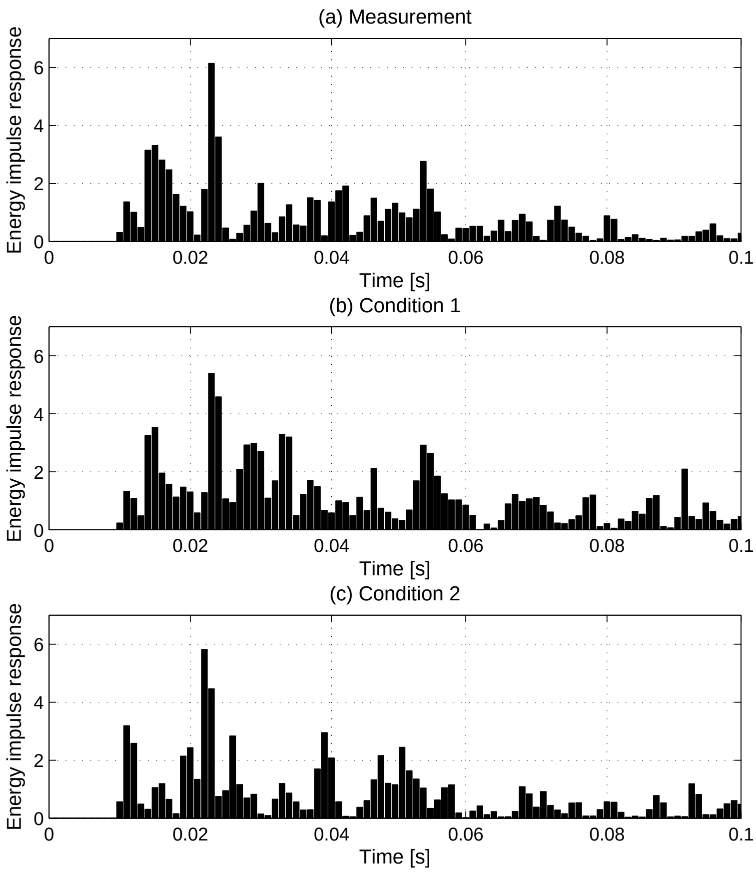

Figure 7.16: Comparison of measured and simulated energy impulse responses at position R4 in the 500 Hz octave band for conditions 1 and 2.

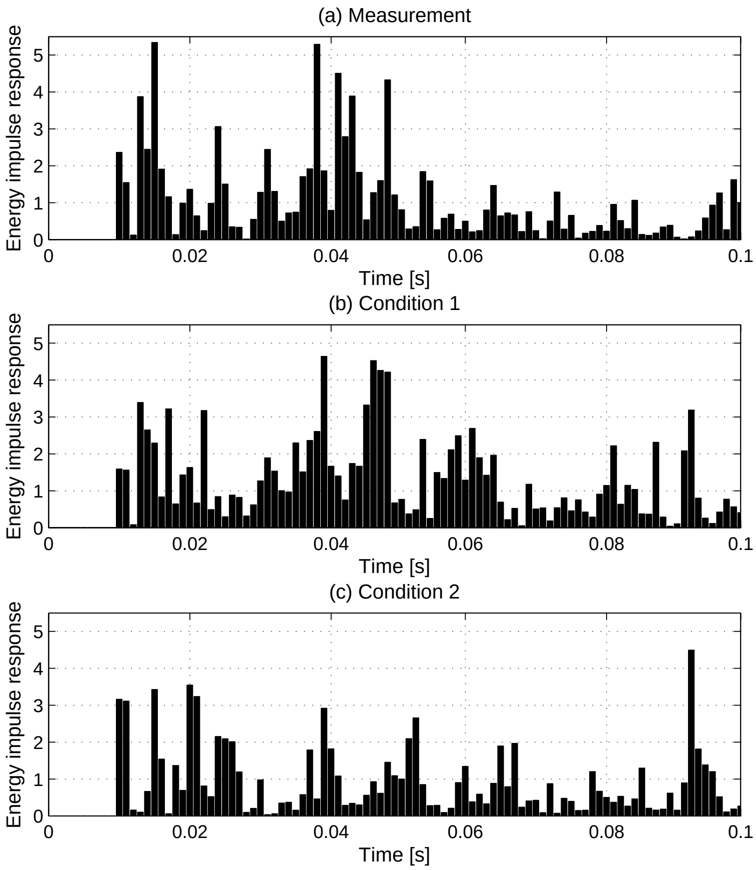

Figure 7.17: Comparison of measured and simulated energy impulse responses at position R4 in the 1 kHz octave band for conditions 1 and 2.

	Error measure E [%]	
Band	Condition 1	Condition 2
125 Hz	65	134
250 Hz	49	95
500 Hz	53	84
1 kHz	63	74

Table 7.2: Error measures E of the simulated energy impulse responses at position 4 in conditions 1 and 2 for the octave bands of 125, 250, 500 and 1k Hz. Computation performed over the initial 50 ms of impulse response.

In light of the results gathered in table 7.2, the implemented model works better with the definition of reflection coefficients as done in condition 1, especially in the octave bands of 250 and 500 Hz.

7.6 Discussion

It has been shown that simulations in condition 1 yield the most accurate results. This suggests that all the materials present in the room should be regarded as acoustically hard when defining the angle independent real-valued reflection coefficient of equation 5.6. Simulations in the rest of conditions lead to less accurate predictions since the reflection coefficients try to model some of the materials or all of them as acoustically soft.

In order to draw solid conclusions based on conditions 2 and 3, materials providing higher absorption should be used. Current materials have absorption values that could be easily comparable to the order of magnitude of the uncertainty due to their characterization.

Best results in the time domain were found for the medium frequency range, namely the octave bands of 250 and 500 Hz. Regarding the errors in the 125 Hz octave band, they could be related to the fact that it is in the low frequency range where the interference phenomena are more noticeable. It may be that the angle independent real-valued reflection coefficient is a too rough approximation of the actual phase shift at each reflection in this frequency range. Furthermore, the errors in this octave band may be partially related to the frequency displacement seen in the frequency responses in figures 7.4 and 7.5, which was localized in this range.

Since the standard listening room is not completely rectangular (whereas that of the simulation is), there exists certain error due to a number of wrongly computed image sources. One could think that the incorrect arrival times of the contributions coming from those wrongly computed image sources could lead to shifted maxima and minima in a frequency response. However that is not believed to be the cause of the frequency displacement since the location of the image sources is frequency independent whereas the displacement seems to be localized within a determined frequency region. On the other hand, the fact that the frequency displacement is shown only for some of the considered conditions suggests that it is related to a wrong modelling of the phase shift by the reflection coefficient.

De Geest and Patzold [1996] reached accurate predictions of frequency responses with their phase RTM in rectangular rooms. On the contrary they observed errors in the frequency responses when attempting to simulate more irregularly shaped rooms. These errors, which appeared especially in the low frequencies (up to around 190 Hz), were attributed to sound diffraction. According to the authors, when not all image sources are visible diffracted energy propagating from visible zones to shadow zones becomes significant, mainly at low frequencies. This suggests that the perceived frequency displacement could be partially due to the diffraction present in the room.

Regarding the representation of peaks and dips in the frequency domain, it has been shown that the implemented model fails to properly represent the dips when no phase shift at reflection is allowed. Conversely, when there is a 180 ° phase shift at reflection the dips are better predicted. Furthermore, higher frequency resolutions for the computation of the simulated transfer functions are expected to provide more accuracy in this respect, in light of the results found in [Jeong and Ih, 2009].

With respect to the pressure impulse responses, early parts were found to be better predicted than late parts, i.e. the transient components due to the early or low order reflections are more accurately simulated. This fact suggests that there is an error existent in the phase shift that a sound wave undergoes in every reflection. This error accumulates as the order of reflection increases, leading to less accuracy in the late part of the simulated impulse responses. In order to prove this, the error measures of the simulated energy impulse responses at point R4 for condition 1 are calculated now for the initial 100 ms. The results are listed in table 7.3 together with those previously listed in table 7.2, which were computed based on the initial 50 ms of the impulse responses.

	Error measure E [%]	
Band	Initial 50 ms	Initial 100 ms
125 Hz	65	81
250 Hz	49	54
500 Hz	53	66
1 kHz	63	83

Table 7.3: Error measures E of the simulated energy impulse responses at position 4 in condition 1 for the octave bands of 125, 250, 500 and 1k Hz. Computations performed over the initial 50 and 100 ms of impulse response.

By comparing both columns in table 7.3, it can be noticed that the error measures increase for all bands when a longer duration of impulse response is considered for the calculations. These results agree with previous findings by Dance et al. [1995]. They showed that the assumption of no phase shift at reflection may be suitable for early reflections from hard surfaces whereas it seems to lead to increasing inaccuracy the greater the contribution of higher order reflections.

The angle independent real-valued reflection coefficient is a rough assumption that cannot fully represent the correct phase shift at each reflection. Taking this into consideration, the implemented model consisting of the PISM with the aforementioned reflection method was found to provide reasonable agreement with measured data in a room presenting acoustically hard surfaces. This fact was also pointed out by Lam [2005], who obtained accurate predictions when using real reflection coefficients with the PISM for a room with low absorptive surfaces.

The performance of the implemented model was shown to be more appropriate at the medium frequency range and particularly in the early part of the impulse responses. This agrees with previous work by Jeong et al. [2008], where similar results were obtained based on a phase BTM using as well the angle independent real-valued reflection coefficient.

The low frequency range can be analysed by means of numerical methods. On the contrary, the high frequency range can be modelled by conventional geometrical acoustic models. The results presented here suggest that the studied model could be a solution for the medium frequency range, corresponding to the octave bands of 250 and 500 Hz.

One advantage of the implemented model is that the only required information from the materials is the absorption data, which is generally easier to obtain than the impedance. Furthermore, since neither complex reflection nor angular dependence is included, the computation time is still affordable for the prediction of early parts of impulse responses.

It would be however interesting to study others of the different methods described in section 5.2 for the modelling of the reflection coefficient. In this way conclusions could be drawn by comparing the results to those found in the present work. In addition, further studies are required with more absorptive enclosures in order to test the reflection methods with different types of materials.

Chapter 8

Conclusion

The sound field in a quasi rectangular room with acoustically hard surfaces has been simulated by means of a model consisting of the PISM with angle independent real-valued reflection coefficients. The performance of the implemented model has been assessed by comparing the simulation results with measurements carried out in the aforementioned room.

The angle independent real-valued reflection coefficient provides a rough approximation of the actual phase shift that is usually produced at the reflection of a sound wave with a wall, allowing either in phase or out of phase reflections. Taking this into consideration, the implemented model was shown to provide reasonable agreement with measured data. Most accurate predictions were found when reflections are modelled in phase. Hence it can be stated that for the considered scenario the phase shift on reflection can be discarded if some error can be accepted.

The performance of the implemented model was shown to be more appropriate at the medium frequency range, namely the octave bands of 250 and 500 Hz. Furthermore, it seems that the assumption of no phase shift on reflection is suitable particularly for the early part of the impulse responses when dealing with reflections from hard surfaces. Conversely, the error was found to increase in the late part of the simulated impulse responses. Therefore more accurate information of the phase shift on reflection is required in order to correctly predict entire impulse responses.

The implemented model presents the advantage of requiring only absorption data from the surface materials, i.e. no impedance information is needed. In addition, it results computationally simple due to the fact that neither complex reflection nor angular dependence is involved.

To conclude, this work has shown that incorporating phase information into the ISM in terms of complex sound pressure propagation and real reflection already provides reasonable predictions of the complex sound field in the considered scenario, notwithstanding the fact that real reflection coefficients cannot fully represent the correct phase shift on reflection. If the accuracy of the results is to be enhanced, more accurate modelling of the phase shift on reflection is required.

8.1 Future Work

Further comparisons of simulations based on different methods of modelling the reflection coefficients can lead to interesting results. This means including angular dependence and complex reflections. As well, considering a more realistic scenario in terms of geometry and materials would be an extension of the implemented model.

Computing objective parameters, e.g. reverberation time, out of the simulated impulse responses for a subsequent comparison with measurements can be another approach for the evaluation of the implemented model or a variation thereof. Furthermore, auralizations based on the measured and simulated impulse responses could be performed in order to assess their perceptual differences. The suggested studies could reveal the importance of the phase information in the respective tasks.

Bibliography

08gr961. Perceptual evaluation of control room design principles, 2008.

AAU Acoustics. Listening room, 2009. URL `http://www.es.aau.dk/sections/acoustics/facilitiesequipment/listening_room/`. Can be found on enclosure CD.

J. B. Allen and D. A. Berkley. Image method for efficiently simulating small-room acoustics. *J. Acoust. Soc. Am.*, 65(4):943–950, 1979.

B&K. B&k 4296 datasheet, 1989.

J. Borish. Extension of the image model to arbitrary polyhedra. *J. Acoust. Soc. Am.*, 75 (6):1827–1836, 1984.

I. Bork. Report on the 3rd round robin on room acoustical computer simulation – part i: Measurements. *Acta Acustica united with Acustica*, 91:740–752, 2005a.

I. Bork. Report on the 3rd round robin on room acoustical computer simulation – part ii: Calculations. *Acta Acustica united with Acustica*, 91:753–763, 2005b.

CATT. *CATT-Acoustic v8.0. User's Manual*, 2002. URL `www.catt.se`. Can be found on enclosure CD.

C. L. Christensen. *ODEON room acoustics program user manual. Version 9.1*, 2008. URL `www.odeon.dk`. Can be found on enclosure CD.

B. Dalenbäck. Room acoustic prediction based on a unified treatment of diffuse and specular reflection. *J. Acoust. Soc. Am.*, 100(2):899–909, 1996.

S. M. Dance, J. P. Roberts, and B. M. Shield. Computer prediction of sound distribution in enclosed spaces using an interference pressure model. *Appl. Acoust.*, 44:53–65, 1995.

E. De Geest and H. Patzold. Comparison between room transmission functions calculated with a boundary element method and a ray tracing method including phase. *Proceedings of Internoise 96*, pages 3177–3180, 1996.

M. E. Delany and E. N. Bazley. Acoustical properties of fibrous absorbent materials. *Appl. Acoust.*, 3:105–116, 1970.

D. Douglas. Transfer-function measurement with maximum-length sequences. *AES Audio Engineering Society*, 37:419–444, June 1989.

M. Garai. Measurement of the sound-absorption coefficient in situ: the reflection method using periodic pseudorandom sequences of maximum length. *Appl. Acoust.*, 39:119–139, 1993.

R. N. Hammad. Simulation of noise distribution in rectangular rooms by means of computer modelling techniques. *Appl. Acoust.*, 24:211–218, 1988.

ISO 3382. Acoustics - Measurement of the reverberation time of rooms with reference to other acoustical parameters, 1997.

C. Jeong and J. Ih. A note on the proper frequency resolution for the room transfer function in the phased beam tracing method. *Appl. Acoust.*, 70:120–128, 2009.

C. Jeong, J. Ih, and J. H. Rindel. An approximate treatment of reflection coefficient in the phased beam tracing method for the simulation of enclosed sound fields at medium frequencies. *Appl. Acoust.*, 69:601–613, 2008.

L.E. Kinsler et al. *Fundamentals of Acoustics*. John Wiley and Sons, Inc., 4. edition, 2000. ISBN 0-471-84789-5.

M. Kleiner, B. Dalenbäck, and P. Svensson. Auralization - an overview. *J. Audio Eng. Soc.*, 41(11):861–875, 1993.

H. Kuttruff. *Room Acoustics*. Elsevier Science Publishers LTD, 3. edition, 1991. ISBN 1-85166-576-5.

H. Kuttruff. *Room Acoustics*. Spon Press, 4. edition, 2000. ISBN 0-203-18623-0.

K. H. Kuttruff. Auralization of impulse responses modeled on the basis of ray-tracing results. *J. Audio Eng. Soc.*, 41(11):876–880, 1993.

Y. W. Lam. Issues for computer modelling of room acoustics in non-concert hall settings. *Acoust. Sci. & Tech.*, 26(2):145–155, 2005.

E. A. Lehmann and A. M. Johansson. Prediction of energy decay in room impulse responses simulated with an image-source model. *J. Acoust. Soc. Am.*, 124(1):269–277, 2008.

E. Mommertz. Angle-dependent in-situ measurements of reflection coefficients using a subtraction technique. *Appl. Acoust.*, 46:251–263, 1995.

PTB. Physikalisch-technische bundesanstalt, working group 1.73, room acoustics α-databank, 2009. URL `http://www.ptb.de/en/org/1/17/173/datenbank.htm`. Can be found on enclosure CD.

V. Pulkki, T. Lokki, and L. Savioja. Implementation and visualization of edge diffraction with image-source method. *J. Audio Eng. Soc.*, Convention Paper 5603, 112th Convention, 2002.

J. H. Rindel. Modelling the angle-dependent pressure reflection factor. *Appl. Acoust.*, 38: 223–234, 1993.

J. H. Rindel. The use of computer modeling in room acoustics. *Journal of Vibroengineering*, 3(4):219–224, 2000.

J. S. Suh and P. A. Nelson. Measurement of transient response of rooms and comparison with geometrical acoustic models. *J. Acoust. Soc. Am.*, 105(4):2304–2317, 1999.

U. P. Svensson and U. R. Kristiansen. Computational modelling and simulation of acoustic spaces. *J. Audio Eng. Soc.*, AES 22nd International Conference on Virtual, Synthetic and Entertainment Audio, 2002.

D. Van Maercke. Simulation of sound fields in time and frequency domain using a geometrical model. *Proceedings of the 12th International Congress on Acoustics (ICA)*, paper E11-7, 1986.

M. Vorländer. Simulation of the transient and steady-state sound propagation in rooms using a new combined ray-tracing/image-source algorithm. *J. Acoust. Soc. Am.*, 86(1): 172–178, 1989.

M. Vorländer. *Auralization*. Springer-Verlag Berlin Heidelberg, 1. edition, 2008. ISBN 978-3-540-48829-3.

Z. Xiangyang, C. Ke'an, and S. Jincai. Modeling the sound fields in rooms with multiple sources using a hybrid image method including phase. *Acta Acustica united with Acustica*, 88:88–92, 2002.

Appendices

Appendix **A**

Measurement of Surface Impedance

This appendix gives a brief insight of different methods of obtaining the impedance of surfaces.

Impedance Tube

The measurement of surface impedance is traditionally made using an impedance tube as described in ISO 10534[†]. However this technique presents several limitations. The working frequency range of the results is limited due to the tube dimensions. It has been stated in [Kuttruff, 2000] that to cover the range from 100 to 5000 Hz two tubes of different dimensions are generally required. On the other hand, the results seem to be sensitive to the mounting of the material under test [Garai, 1993] and last but not least, it can happen that there is no material sample available to be mounted into the tube.

In Situ Techniques

The latter suggests the consideration of in situ techniques. The complex reflection coefficient can be measured in situ by means of the so-called *reflection* method, by detecting the signal impinging on and reflecting from the surface under test.

A setup consisting of a loudspeaker facing a microphone in front of the surface under test is arranged. The impulse response is measured and shall contain direct sound, reflection from the surface under test and eventually other parasitic reflections from other surfaces. The reflection coming from the surface under test must be isolated from the global response. There are several ways of performing this task. For instance, the reflected impulse may be selected by multiplication with an adequate window in the time domain [Garai, 1993]. A more sophisticated approach is to cancel the direct sound out by subtraction [Mommertz, 1995]. This involves that the incident impulse must be exactly known. Normally it is measured in pseudo-free-field conditions by locating the loudspeaker-microphone arrangement far from reflecting surfaces. Next, the parasitic reflections must be gated out by multiplication of the reflected impulse with a suitable window.

[†]There are also other techniques based on impedance tube apart from that described in ISO 10534.

By Fourier transforming the isolated reflection, the complex frequency dependent reflection coefficient of the surface under test is obtained. Hence the surface impedance can be deduced. Both methods present certain advantages and limitations. In both of them the response of the transmission system, mainly the loudspeaker, must be accounted for. As well, it must be noted that both methods assume plane wave propagation. While this is true for the impedance tube based methods, spherical wave fronts are present instead when measuring in situ. Therefore it must be considered whether the wave fronts can be regarded as plane.

In the subtraction method the microphone can be positioned very close to the surface. This fact should increase the delay between the reflected impulse and the parasitic reflections, thus allowing the usage of a larger window length to isolate the former, which is advantageous. On the other hand, non complete cancellation of the direct sound may affect the results at high frequencies. There are several other considerations that must be taken into account when applying the aforementioned methods that will not be described here.

Other Approaches

Another possibility to substitute complex impedance measurements is gathering those values from empirical relations, for instance those developed by Delany and Bazley [1970]. In that study, the acoustical characteristics of a number of fibrous absorptive materials covering a wide range of flow-resistance, σ, values were measured by the impedance tube method. These data were normalised in terms of the variable frequency/flow-resistance and subsequently represented as empirical relations. The relations require solely knowledge of the flow-resistance of the material under consideration. Should such a parameter not be available, an estimation of its order of magnitude can be found in the aforementioned study for a number of materials.

Appendix B

Measurement Report: RIRs at the Standard Listening Room

Purpose

This measurement report describes the procedure followed to obtain the RIRs at the standard listening room. Such a room is used as case study and the measurements carried out in it are to be compared with the simulation results, thus allowing an evaluation of the implemented algorithms.

Measurements described were conducted with inspiration on the guidelines in the ISO 3382 standard [ISO 3382, 1997].

Measurement Setup

Measurements took place in a standard listening room which conforms with the IEC 60268-13 standard, that describes an average living room acoustically [AAU Acoustics, 2009]. It is located at Aalborg University, Fredrik Bajers Vej 7 B4-207, 9220 Aalborg, Denmark. The measurements were carried out on the 14th of May, 2009.

Room Overview

The dimensions of the standard listening room are 7.8 m long, by 4.14 m wide, by 2.76 m high yielding a volume of 89 m^3 and the room can be seen in several pictures in figure 7.1, showing the details pointed out in the following. The walls are concrete made, except a little window of around 0.34 m^2 at wall $y = 0$ (see figure B.1) and an area made of plaster of around 2.15 m^2 in the centre of wall $y = 7.8$. Furthermore, there is a double door with metallic coverage from the inside located at wall $x = 4.14$. There are also several connection panels and plastic ducts with rectangular section housing wires inside.

The floor is wooden made, except for a little area of glazed tile at the end of the dimension y with a surface of around 3 m^2, occupying the whole room width. For the measurements however the floor was covered with carpet. Most of the floor surface was covered with one carpet, but there was an area of around 6.2 m^2 that had to be covered with other types of carpet.

The ceiling is made of chip wood boards located at a height of 2.76 m above the floor, which are suspended from a concrete ceiling at 3.05 m above the floor. Originally the series of boards next to the walls $x = 0$, $x = 4.14$ and $y = 0$ were located obliquely. For the measurements, those parts were arranged so that the boards were located horizontally. It must be noted that the structure for the holding of the former oblique boards was still present when the measurements were carried out.

The room presents thus a shoebox shape, except for an oblique chip wood surface of around 2 m^2 hiding a pipe from the ventilation system, which is located at the top of wall $x = 4.14$ and occupies half of its length.

Room Conditions

During the measurements the room was unoccupied. Nothing out of the normal was present in the room apart from the aforementioned details.

The temperature at the beginning of the measurements was 22° C and the humidity 27%.

Source and Microphone Positions

The measurement setup considered is based on a source located at position S1 and a microphone located at positions R1-R6. The scale sketch plan of the room including source and microphone positions is depicted in figure B.1 and the coordinates of every position are listed in table B.1.

Position	x [m]	y [m]	z [m]
S1	3.00	1.50	1.50
R1	1.50	1.50	1.27
R2	1.50	6.30	1.27
R3	3.00	6.30	1.27
R4	1.00	3.90	1.27
R5	2.07	5.00	1.27
R6	2.65	3.00	1.27

Table B.1: Source and microphone position coordinates (see figure B.1 for origin of coordinates). The magnitude z corresponds to the height above the floor.

Regarding source position S1, the height z is given for the centre of the loudspeaker. With respect to microphone positions (R1-R6), the height z is given for the top of the microphone.

These positions were selected to have some meaning. One-dimensional reflections taking place along x and y direction are expected to be dominant at positions R1 and R3 respectively. R6 and mainly R2 which is in a diagonal way from S1 should not be

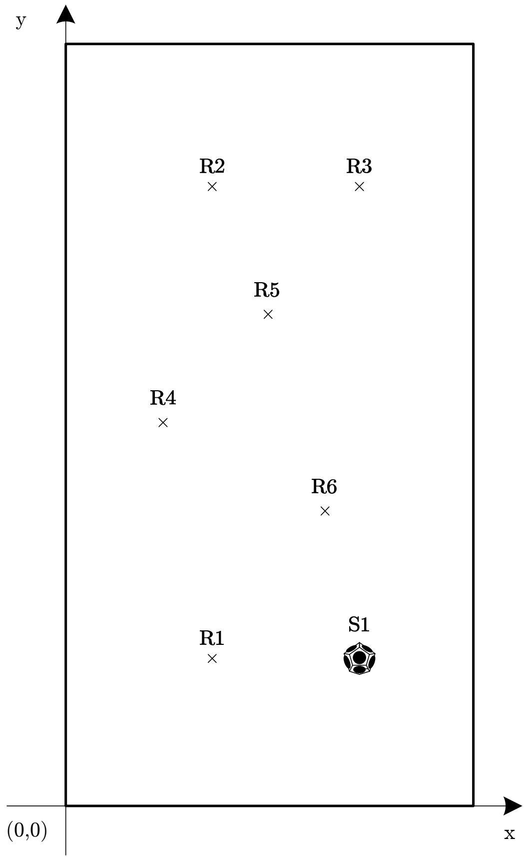

Figure B.1: Sketch plan of the room with source and microphone positions.

strongly affected by them. Lastly R4 and R5 are located at half the length and width of the room respectively. Hence it is expected they are influenced to a great extent by axial room modes parallel to directions y and x respectively. Furthermore, the height of the microphone was determined as 1.27 m so as to emulate a sitting posture [Jeong et al., 2008].

Based on the aforementioned setup, six RIRs were acquired.

Equipment

The equipment used is listed in table B.2.

B&K 4134 is the omnidirectional measurement microphone used to acquire the RIRs. Since it is a pressure field microphone, it must be placed vertically (90° with respect to source horizontal axis).

The sound source B&K 4296 is an omnidirectional source made of twelve loudspeakers

Item	Type	AAU LBNR
Measurement microphone	B&K 4134	08130-00
Mic. preamplifier	B&K 2619	07797-00
Microphone power supply	B&K 2804	06998-00
Microphone calibrator	B&K 4230	08155-00
Loudspeaker	B&K 4296	33950
Power amplifier	Rotel RB-976 Mk II	33975-00
Measurement system	01 dB Harmonie	56524-00
Laptop	Fujitsu	47220-00
Temperature/Humidity Sensor	Kane May 8004	33192-00

Table B.2: Measurement equipment.

in a dodecahedral configuration that radiates sound evenly with a spherical distribution [B&K, 1989].

Measurement Method

Excitation Signal

RIRs were measured by means of the maximum-length sequence (MLS) technique. The excitation signal consists of a binary sequence whose spectrum can be considered white. White spectrum signals allow using cross-correlation function to obtain the impulse response of the system. This signal is deterministic and periodic, meaning that it can be exactly repeated and used in analysis.

Analysis Technique

The idea is to apply an MLS signal to the system. The sought broadband impulse response is computed by cross-correlating the measured response with the excitation signal. This technique is proved to be highly efficient compared to others such as TDS and dual channel FFT systems. Good results are obtained in terms of computation efficiency as well as improved signal to noise ratio [Douglas, 1989].

Measurement System: 01 dB Harmonie

The measurement system consists of a data acquisition unit which transfers data in real time to a computer via a PCCard (former PCMCIA) interface. The acquisition unit provides connections for four input channels, two dual channel outputs and digital input/outputs. The computer is the host of the acquisition unit. The system is controlled and configured by means of software. For the measurements of this report, the software used was dBBATI32 which is a building acoustics analyser. Following considerations in the setup were taken into account.

- **Acquisition order**: The MLS signal order m, can be chosen to be up to 18, leading to a sequence period of 262144 samples. The sampling frequency determines the length of those periods in time. This length must be longer than the expected duration of the impulse response in order to avoid time aliasing phenomena.
- **Sampling frequency**: The system allows sampling frequencies up to 51.2 kHz.
- **Number of averages**: The system averages up to 2048 acquisition periods before computing cross-correlation. This operation increases the signal to noise ratio. A pre-average of 16 MLS periods leads to a signal to noise ratio improvement of 12 dB.

Measurement Procedure

Equipment Setup

The signal flow diagram is shown in figure B.2.

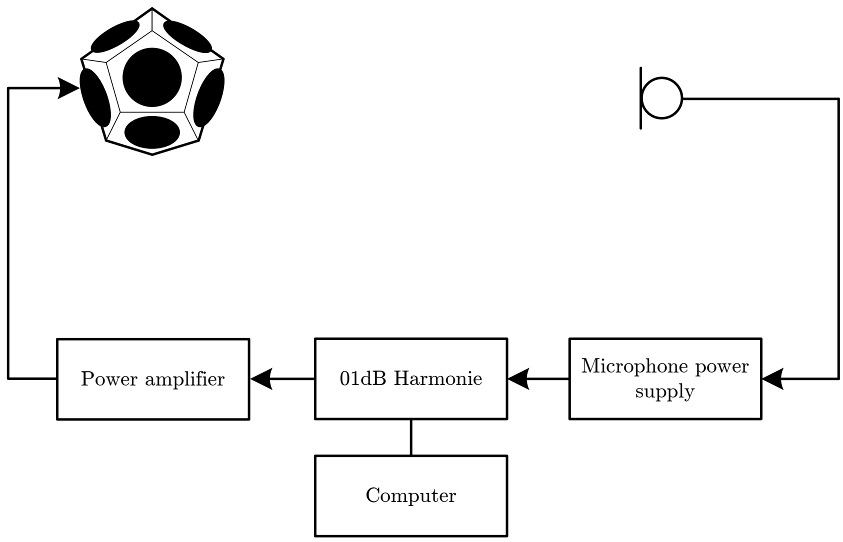

Figure B.2: Signal flow diagram among equipment during measurements.

01 dB Harmonie

The microphone and calibrator were specified in the hardware configuration and the system was set as shown in table B.3 following previous considerations for its setup.

Parameter	Value
Acquisition order	17
Sampling frequency	51.2 kHz
Number of averages	16
Frequency range	20 kHz

Table B.3: 01 dB Harmonie setup.

For the MLS signal a 17 acquisition order was selected, leading to a period of 131072 samples (2560 ms for a sampling frequency of 51.2 kHz).

Procedure

1. Connection of all the equipment as shown in figure B.2.
2. Setup Harmonie according to table B.3.
3. Arrangement of setup according to figure B.1 and table B.1.
4. Microphone calibration.
5. Measurement of temperature and humidity.
6. Measurement of RIRs at positions R1-R6.

Results

Based on the setup described above, six RIRs were acquired. As an example, RIR obtained at the position R3 is shown in figure B.3.

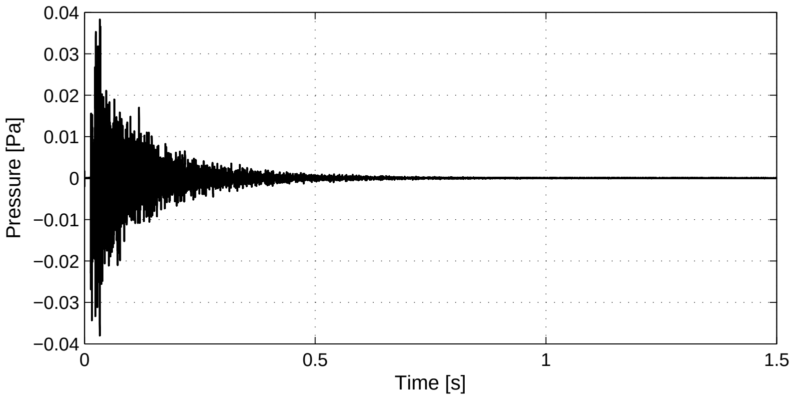

Figure B.3: RIR measured at position R3 at the standard listening room.

Enclosure: CD

A CD-ROM is attached as enclosure. This CD-ROM contains information to be studied if the reader desires additional insight into the different topics of the report.

Contents of the CD:

- Project Report (PDF & PS format).
- Internet bibliography.
- Matlab scripts.
- Measurements at the standard listening room.